

Transfer Learning Applied to Stellar Light Curve Classification

Cunshi Wang^{1,3,2}, Yu Bai^{1,3}, Hengpeng Han¹, Huiqin Yang^{1,3}, and Jifeng Liu^{1,3,2,4}

¹ Key Laboratory of Optical Astronomy, National Astronomical Observatories, Chinese Academy of Sciences, 20A Datun Road, Chaoyang District, Beijing 100101, People's Republic of China

² College of Astronomy and Space Sciences, University of Chinese Academy of Sciences, Beijing 100049, China

³ Institute for Frontiers in Astronomy and Astrophysics, Beijing Normal University, Beijing 102206, China

⁴ New Cornerstone Science Laboratory, National Astronomical Observatories, Chinese Academy of Sciences, Beijing 100101, People's Republic of China

Received September 15, 1996; accepted March 16, 1997

ABSTRACT

Context. Variability carries physical patterns and astronomical information of objects, and stellar light curve variations are essential to understand the stellar formation and evolution processes. The studies of variations in stellar photometry have the potential to expand the list of known stars, protostars, binary stars, and compact objects, which could shed more light on stages of stellar lifecycles.

Aims. The progress in machine-learning techniques and applications has developed modern algorithms to detect and condense features from big data, which enables us to classify stellar light curves efficiently and effectively. We explore several deep-learning methods on variable star classifications.

Methods. The sample of light curves is constructed with δ Scuti, γ Doradus, RR Lyrae, eclipsing binaries, and hybrid variables from *Kepler* observations. Several algorithms are applied to transform the light curves into images, continuous wavelet transform (CWT), Gramian angular fields, and recurrent plots. We also explore the representation ability of these algorithms. The processed images are fed to several deep-learning methods for image recognition, including VGG-19, GoogLeNet, Inception-v3, ResNet, SqueezeNet, and Xception architectures.

Results. The best transformation method is CWT, resulting in an average accuracy of 95.6%. VGG-19 shows the highest average accuracy of 93.25% among all architectures, while it shows the highest accuracy of 97.2% under CWT transformation method. The prediction can reach ~ 1000 light curves per second by using NVIDIA RTX 3090. Our results indicate that the combination of big data and deep learning opens a new path to classify light curves automatically.

Key words. Stars: variables: general — Methods: data analysis

1. Introduction

Photometric variability is a common aspect of many astronomical objects, and the mechanism behind it is one of the most essential pieces of knowledge in astrophysics. Variable stars have played a significant role in time-domain astronomy for a long time, and the latter has emerged as a critical field of current astronomy and astrophysics. Cepheid variables, (Eddington 1917; Pierce et al. 1994; Stetson 1996), are a type of pulsating variable stars, and serve as standard candles to calculate distances to galaxies and even on a cosmological scale. Pulsating variable stars mainly include bright Asymptotic Giant Branch (AGB) Classical Cepheids, multi-mode pulsating RR Lyrae (RR), fast pulsating δ Scuti stars (δ Sct) and γ Doradus stars (γ Dor). They have different absolute magnitudes, pulsation modes, and mechanisms, representing different period-luminosity relations (Sterken & Jaschek 2005; Percy 2011). The classification of variable stars, especially pulsating variables, has helped us understand the stellar formation and evolution, as well as the structure and combination of binaries and n-body systems (Prša et al. 2011; Slawson et al. 2011; Matijević et al. 2012; Conroy et al. 2014b,a; LaCourse et al. 2015; Kirk et al. 2016; Abdul-Masih et al. 2016).

However, modern astronomy has entered the big data era. For example, the Zwicky Transient Factory (ZTF, Bellm 2014), a time-domain survey at Palomar Observatory, uses a 1.2m tele-

scope with a $47deg^2$ field of view to scan the sky every two days. ZTF produces about 1TB raw uncompressed data each night (Mahabal et al. 2019). SiTian (Liu et al. 2021), will use an array of more than one hundred 1-meter telescopes with a super-large field of views, deployed worldwide to monitor the sky in g , r , and i bands. It will monitor more than $1,000deg^2$ of the sky every 30 minutes, and generate raw data in a count of 40GB per minute. The processed data will be an estimated total of about 140TB per night.

Machine-learning, especially deep-learning are the solutions of big data analytics, and they have shown obvious advantages in many realms, such as image processing (Simonyan & Zisserman 2015; Szegedy et al. 2014, 2015; He et al. 2015; Iandola et al. 2016; Chollet 2017), translation (Vaswani et al. 2017), control theory (Qu et al. 2020; Li & Han 2022), medical (Zhang et al. 2019), and infrastructure construction (Bai et al. 2020; Mohammadpourfard et al. 2021). The sub-realms of image processing, include image labeling (Huang et al. 2019a), or screen segmentation (Fu et al. 2019; Huang et al. 2019b), which have been applied to facial discrimination and automatic driving. In astronomy, machine-learning techniques also exhibit the mighty ability to process raw data from the newest large telescopes, including object or image morphology classifications (Bertin & Arnouts 1996; Bellm 2014; Schutter & Shamir 2015; Hinnert et al. 2018; Barchi et al. 2020; Wang et al. 2022), and parameter regressions (Arjona & Nesseris 2020; Yang et al. 2021; Galarza et al. 2022).

Machine learning is based on statistics, theorem of optimization, and computer science. The algorithms aiming at different goals apply different loss functions and perform optimization to minimize the loss. The k -nearest neighbor (k -NN) algorithm (Cover & Hart 1967; Stone 1977) claimed that the label of an object is determined by the labels of the k -th nearest objects by calculating their distance. Quinlan (1986) applied a tree plot to help with classification and introduced information entropy to guide the tree's split. Cortes & Vapnik (1995) introduced the idea of using a hyper-plane with the maximum distance for binary classifications. In these machine-learning algorithms, the input features are selected manually and then fed to algorithms. However, the features of images cannot be manually selected, for they are large matrices with thousands of elements. Traditional machine learning methods are efficient in solving problems with several parameters, but are difficult to extract important features from data with large dimensions. The key to applying machine learning to the image's domain is selecting and condensing the features.

Convolution is the answer. It concentrates information on an image area by pointwise multiplication. The information then transfers to the activation function that outputs more essential features. To condense the features, the output flows into a max-pooling to select the main feature in an area of the image. These formed the earliest Convolutional Neural Network (CNN) LeNet (LeCun et al. 1995, 1998, 2015).

CNN evolved quickly, along with the appearance of many new ideas and the formation of new architectures. Simonyan & Zisserman (2015) claimed that a deeper network would present better training results. He & Sun (2014) argued that a deeper network might come up with a degeneration problem, and result in lower accuracy. In order to solve this degeneration problem, He et al. (2015) introduced the structure of residual connection. This structure connected the upper layer to the lower layer. Szegedy et al. (2014) proposed that putting convolutions with all sizes or any other processes together to form an inception block, would perform better than a single convolution block. This method evolves and has become one of the important ideas in the architectures of CNNs (Szegedy et al. 2015; Chollet 2017).

Training a CNN usually consumes a huge computational costs, while transfer learning provides us with a more efficient way. Transfer learning (Pan & Yang 2010) is a technique that adapts a pre-trained model to a new domain. It is commonly used in deep learning applications. We could quickly transfer learned features to a new task using a smaller number of training images. By replacing the fully connected (FC) layer and classification layers, we can transfer the knowledge from image recognition to light curve classification.

ZTF has applied machine learning to classify the transient objects and has presented the detection and classification of moving objects (Mahabal et al. 2019). Duev et al. 2019 applied a CNN architecture to identify fast-moving objects from ZTF. The study has proved that CNN can achieve the goal of 50 times faster than the random forest algorithm. ZTF also applied a machine-learning based point-source classifier to its pipeline. The classifier links a real-bogus detector to output reliability scores of the source (Masci et al. 2018). The pipeline also contains a streak diagnostics module and a stellar-galaxy classification module that applies the machine-learning scores.

SiTian project will produce about 140 times more data per night than ZTF. A more effective and efficient pipeline is in great demand to detect transient objects, and do variable identification and classification. Deep learning has provided opportunities for

automatic feature extraction and classification in large astronomical data sets.

In this work, we investigate various deep learning architectures to address the classification of variable stars in the *Kepler* dataset. The top-performing architectures will be tested on mock light curves in the mini-Sitian catalogs to assess their effectiveness and provide insights. The light curves are selected from *Kepler* Observations, including *Kepler* and *K2* data (Section 2.1). We choose different kinds of Cepheid Variables, including RR (Section 2.3), δ Sct (Section 2.4), and γ Dor (Section 2.5). We also select the eclipsing binaries (EB) from *Kepler* archive data in Section 2.2. The variables with multiple classes in literature are defined as Hybrids (HYB, Section 2.6). The training catalog construction is presented in Section 2.7. We then reform the light curves, and make the pre-processing step of our training catalog (Section 2.8). In order to transform the light curves into images, we apply three algorithms: the Continuous Wavelet Transform (CWT, Section 3.1), Gramian Angular Fields (GAF, Section 3.2), and Recurrent Plot (RP, Section 3.3). These transformations yield the training sample, making them adapted to the CNN algorithms. In Section 4, we adopt different algorithms for classification, including the VGG-19 (Section 4.1), the GoogLeNet (Section 4.2), the Inception-v3 (Section 4.3), the ResNet-101 (Section 4.4), the SqueezeNet (Section 4.5), and the Xception (Section 4.6). The result is presented in Section 5, including a blind test with Transiting Exoplanet Survey Satellite (TESS) data to evaluate the generalization ability (Section 5.3). We discuss the representation ability of transformation methods (Section 6.1), and compare our result with that of a simple CNN algorithm (Section 6.2). In Section 6.3, we discuss two new methods that are also appropriate to light curve classification. We also present a prospect of deep learning in SiTian.

2. Variable types and Data reduction

The reasons of variability could be intrinsic or extrinsic. One classification system is rotation (ROT), eclipsing binary, pulsating variables, eruptive variables, and other-type variables (Sterken & Jasnsek 2005; Percy 2011).

We focus on eclipsing binaries and pulsating variables, including RR, δ Sct, and γ Dor. The objects with more than one class in literature are all labeled with Hybrid (HYB). Classical Cepheid variables are precluded from our sample, since their sample size is too small for classification.

2.1. *Kepler* and *K2* mission

The *Kepler* spacecraft was launched in 2009, aiming to search for Earth-like planets (Borucki et al. 2010). It carried an optical telescope with a 95cm aperture and a 115.6 deg^2 field of view, presenting light curves of 200,000 targets with unprecedented precision. Such high precision has helped to discover more than 2,000 planets. For stars with V band magnitude from 13-14, it had a precision of 100 ppm. For stars with V band magnitude from 9-10, it had a precision of 10 ppm.

Kepler has lost half of the four reaction wheels, ends the four-year mission, and starts the *K2* mission. *K2* applied the transit method to detect the photometric variability of the stars near the ecliptic plane and provided catalogs with a similar photometric precision. The observations of *K2* were controlled by the remaining reaction wheels and the thrusters, and each campaign is restricted to 80 days.

Two kinds of light curves were provided, Presearch Data Conditioning (PDC) and Simple Aperture Photometry (SAP)

light curves (Van Cleve & Caldwell 2016). SAP light curves are the summing of all pixel values in a pre-defined aperture. In contrast, PDC light curves were generated by *Kepler* Operation Science Center by removing the effects of systematic errors. In this work, we adopt PDC light curves.

Meanwhile, there are two kinds of data with different time resolutions. One is long-cadence data, which have a 30 minutes sampling interval. The other is short-cadence data with a one-minute sampling interval. Considering the limited number of short-cadence data, we focus on the long-cadence light curves. Based on the *Kepler Data Integration Platform* built by Yang & Liu (2019), we remove the difference between each quarter and convert the flux into relative flux. For each light curve pieces, we adopt a polynomial fitting to avoid the influence of the outliers, and then calculate the mean values of the polynomials. The light curves are normalized to ppm by decreasing the mean value, then dividing by the mean value. This process is similar to the process in Han et al. (2021).

2.2. Eclipsing Binary

Eclipsing binaries have near edge-on orbits where the components undergo mutual eclipse, and their classifications are morphological (Percy 2011). The eclipse causes light curve variations, which are tightly related to stellar radii, masses, and luminosity ratios.

Eclipsing binaries can be classified as EA, EB or EW types based on different shapes of light curves. The light curves for the EA type remain almost unchanged between the two eclipses. The light curves exhibit variations between eclipses for the EB type due to the ellipsoidal shape of components. EW type eclipsing binaries have contracting ellipsoidal components, and their light curves show quasi-sinusoidal modulations. In this work, we don't focus on sub-type classification.

2.3. RR Lyrae

RR Lyrae, which can be used as standard candles to build the cosmic distance ladder, are pulsating variables located at the end of the Cepheid instability strip in the Hertzsprung-Russell (H-R) diagram. They are A5 to F5 stars with the absolute magnitude of ~ 0.5 mag, the mass of $\sim 1M_{\odot}$, and low metal abundances ($[Fe/H] \sim 0.0001 - 0.001$ dex) lying in the horizontal branch. The pulsation of RR Lyrae has a period of about 0.1 to 1 day and an amplitude of $0.3 \sim 1.5$ mag in V-bands (Percy 2011).

RR Lyrae finishes the core hydrogen burning and begins the core helium and shell hydrogen burning. The expansion is due to the radiation block, and the gravity causes the contraction, forming the periodic pulsations. RR Lyrae can be divided into several sub-types from RRa to RRd. RRa and RRb have longer pulsating periods compared to others. Typically, RRa has larger pulsating amplitudes and more asymmetrical light curves compared to RRb. RRc has a shorter pulsating period and sinusoidal light curves. Meanwhile, they pulsate in different modes.

2.4. δ Scuti

δ Sct, also termed as dwarf Cepheid, is the most numerous Cepheid variable, located at the bottom of the Cepheid instability strip crossing the main sequence in the H-R diagram (Percy 2011; Dupret et al. 2005). They are usually A5 \sim F8 giants or main-sequence stars with a pulsating period of about $0.03 \sim 0.3$ days. Most δ Scts are in the stage of core hydrogen burning.

The classification of sub-types of δ Sct depends on pulsation amplitudes and metal abundances, such as High-amplitude δ Sct (HADS) or multitude of relatively low amplitude modes (MULT). δ Sct has several pulsation modes, including p modes and g modes, and non-radial modes. It follows the cooler pulsates in fundamental mode. This work does not distinguish the sub-types of δ Sct.

2.5. γ Dor

γ Dors are F0 to F2 stars that are situated at the bottom of the δ Sct instability strip in the H-R diagram (Percy 2011). Their masses are from 1.4 to $2.5 M_{\odot}$, and effective temperatures are from $6500K$ to $8500K$. γ Dors have a longer pulsating period (from 0.3 to 3 days) and lower temperature than δ Sct. They pulsate in non-radial gravity modes (g modes) driven by the convective blocking mechanism (Dupret, M.-A. et al. 2004). Their pulsation differs from δ Sct in pressure mode (p mode) or mixed character modes (Dupret et al. 2005).

2.6. Hybrid

The label HYB in the input catalog contains δ Sct/ γ Dor hybrids and multi-classified variables. For example, the binaries include a δ Sct, γ Dor, and ROT (Bradley et al. 2015; Balona 2018). The instability strips of δ Sct and γ Dor overlap in the H-R diagram, and the stars inside the overlapping zone are δ Sct/ γ Dor hybrids. These hybrids have both characteristics of δ Sct and γ Dor, and their pulsation modes contain both high-frequency p mode and low-frequency g modes (Xiong et al. 2015; Xiong et al. 2016; Sanchez Arias, J. P. et al. 2017).

2.7. Input catalog

The input catalog is built from several catalogs based on *Kepler* archive data. The construction of the input catalog is shown in Table 1.

General Catalog of Variable Stars (GCVS¹, Kholopov et al. 1988; Durevich et al. 1994; Artyukhina et al. 1995; Samus et al. 2021) is a database of variable stars providing by the Sternberg Astronomical Institute and Institute of Astronomy (Russian Acad. Sci.). GCVS presents 6 δ Sct, 21 hybrid variables, and one classic Cepheid.

Molnar et al. (2018) presents 1,391 RR from cross-matching with *Gaia* DR2, including 42 from *Kepler*, and 1,349 from *K2*. The purity of this catalog is about $92\% \sim 98\%$ by using several ready-made codes for search and identification between their work and *Gaia* DR2. We adopt 42 RR after cross-matching with the *Kepler* catalog (Molnar et al. 2018). The catalog includes one classic Cepheid and one Type II Cepheid (T2CEP).

Kepler Eclipsing Binary Star catalog (KEB, Prša et al. 2011; Slawson et al. 2011; Matijević et al. 2012; Conroy et al. 2014b,a; LaCourse et al. 2015; Kirk et al. 2016; Abdul-Masih et al. 2016) presents 2,908 EB from *Kepler* and *K2* surveys. They are given by Eclipsing Binaries via Artificial Intelligence, a neural network that can output EB parameters from given light curves.

Bradley et al. (2015) presents 82 δ Sct, 204 γ Dor and 32 hybrid stars from *Kepler* data. The HYB includes δ Sct/EB, δ Sct/ γ Dor and δ Sct/ROT hybrids.

Balona (2018) provides 1,307 δ Sct, 738 γ Dor and 429 δ Sct/ γ Dor hybrids from *Gaia* data release two to investigate the

¹ <https://heasarc.gsfc.nasa.gov/W3Browse/all/gcvsevars.html>

mechanisms of low-frequency pulsations. The classification of δ Sct and γ Dor is based on frequencies and amplitudes.

2.8. Pre-processing algorithm

A pre-processing step is constructed to manage and clean the light curves for our sample set (Figure 1, upper panel). It can help us to magnify the features and enlarge the training sample. We first delete one CEP and one T2CEP object to avoid an extremely biased training sample. A biased sample may cause great uncertainty in the result (Shalev-Shwartz & Ben-David 2014). We treat the stars with multi-label in different catalogs as hybrids and assign them to class HYB. This process makes the class HYB contain more 'others' type objects.

To fully use each quarter of *Kepler* observation, we divide each quarter's observations into partitions, and each partition will be treated as a sample in our training set. The shortest continuous observation time without any gaps in all light curves is ~ 20 days. We adopt a 10-day partition, half of the shortest continuous observations, and get 1 \sim 9 partitions from each quarter.

The *Kepler* cadence is 30 min, while there are observation gaps in most quarters. The period of the variables are mainly ~ 0.5 days. The stellar light curves with a gap of more than half of this period are difficult to interpolate and are removed to avoid additional noise. We then interpolated all the partitions with a time sequence of 0.02-day (~ 30 min) intervals. The light curves are then normalized between zero and one. The output of the pre-processing algorithm is the input of our transformation methods, which transform light curves into images (Figure 1, middle panels). Table 2 lists out our sample size.

3. Transform light curves into images

Light curves are essential for the studies of variable objects. Types, periods, amplitudes, and oscillation modes enable us to understand their background natures. However, the extraction of these parameters is high computational costs, especially for big data. CNN is a powerful tool to extract and recognize features, since it can learn more robust deep features (Zhao et al. 2017; Sadouk 2018; Tang et al. 2020). Most CNN works more efficiently on two-dimension images than one-dimension series. Several transformation methods have been explored in this section, including CWT, GAFs, and RP. Then the pre-trained models are applied to the outputs of these transformation methods (Figure 1, bottom panels).

3.1. Continuous Wavelet transform

Fourier transform (Equation 1, i stands for the imaginary unit) is one of the most powerful analytical tools in mathematics, which is widely applied in numerical algorithms, analysis, differential equations, and time series analysis. In signal analysis, it can decompose functions depending on space or time (the ' x ' in Equation 1) into functions depending on the spatial frequency or temporal frequency (the ' ξ ' in Equation 1). In variable star analysis, a traditional method is Fourier transform (Sterken & Jaschek 2005; Percy 2011). Deb, S. & Singh, H. P. (2009) applied Fourier decomposition to classify light curves of variable stars.

$$\hat{f}(\xi) = \int_{-\infty}^{\infty} f(x)e^{-2\pi i x \xi} dx \quad (1)$$

However, the Fourier transform has its limitations. It cannot handle the signal whose frequency changes with time. It

presents each frequency component rather than a time-frequency diagram. Fourier transform could not deal with a sudden change in frequency owing to its unattenuated basis on \mathbb{R} .

$$\hat{f}(a, \tau) = \frac{1}{\sqrt{a}} \int_{-\infty}^{\infty} f(t) \Psi\left(\frac{t-\tau}{a}\right) dt \quad (2)$$

Wavelet transform, a Fourier-related transform, solves these problems by shifting and scaling of fast decaying wavelet basis (Equation 2). In the equation, $a \in \mathbb{R}^+$ is the scale (frequency), and $\tau \in \mathbb{R}$ is the translational value (time). The wavelet Ψ belongs to both $L^1(\mathbb{R})$ -space and $L^2(\mathbb{R})$ -space. Further, it is identical in $L^2(\mathbb{R})$ -space (Equation 3).

$$\begin{cases} \int_{-\infty}^{\infty} |\Psi(t)|^2 dt = 1 \\ \int_{-\infty}^{\infty} |\Psi(t)| dt < \infty \\ \int_{-\infty}^{\infty} \Psi(t) dt = 0 \end{cases} \quad (3)$$

CWT shifts the translational value along the time of the signal. Shifting is done again when the scale enlarges to $2a$ (twice the scale). Then the equivalent frequency is reduced to a half, defined as an octave. The CWT also divides an octave into several voices, and the scale of n -voice per octave follows $a, 2^{\frac{1}{n}}a, 2^{\frac{2}{n}}a, \dots, 2^{\frac{n-1}{n}}a, 2a$ inside an octave. The more voice per octave, the finer the scale discretization. Wavelet transform can provide a scalogram, showing the relations among frequencies, times, and magnitudes.

We choose Morse wavelet² (Olhede & Walden 2002; Lilly & Olhede 2008, 2010, 2012) with 12 voice per octave to transform our light curves into images. The horizontal axis of the CWT scalogram shows the time scale, and the vertical axis shows the frequency. Some examples are shown in Figure 2 and Appendix A.

3.2. Gramian Angular Field

We explored GAFs to transform the light curves into images (Wang & Oates 2015), including Gramian Difference Angular Field (GADF) and Gramian Summation Angular Field (GASF). Wang & Oates (2015) tested GAFs and Markov Transition Field (MTF) to evaluate the representation of time series in Tiled CNNs (Ngiam et al. 2010), and concluded that MTF has lower classification accuracy than GAFs in 20 sets of time series. Chen et al. (2015) concluded that the consequence is caused by the uncertainty of inverse calculation in MTF. Ahmad et al. (2021) also supported their conclusion based on the multi-data set classification of the electrocardiogram. Therefore, we adopt GAFs and preclude MTF. The GAF algorithms have been widely applied to diagnosis for railway Wheel flat (Bai et al. 2020), myocardial infarction detection (Zhang et al. 2019), and attack detection of smart grid (Mohammadpourfard et al. 2021).

GAFs embed a time series into a polar coordinate system and calculate the relation between each point by adding their cosine values or decreasing their sine values. The first step of GAFs is a min-max normalizing $\tilde{x} = \frac{x - \min(x)}{\max(x) - \min(x)}$, where x is a column vector of the time series with equal time interval. Then the normalized \tilde{x} is embedded into an identical circle (Equation. 4).

$$\begin{cases} \phi_i = \arccos \tilde{x}_i \\ r_i = \frac{t_i}{n} \end{cases} \quad (4)$$

² <http://jmlilly.net/software>

Table 1. Input catalog

	δ Sct	EB	γ Dor	RR	HYB	CEP
GCVS	6	0	0	0	21	1
Bradley et al. (2015)	82	0	204	0	32	0
Molnar et al. (2018)	0	0	0	1,391	0	2
Balona (2018)	1,307	0	738	0	429	0
KEB	0	2,908	0	0	0	0

Notes. The input catalog. EB stands for eclipsing binary, not the variable type semi-detached eclipsing binary. RR stands for RR Lyrae, and HYB for all hybrid types. CEP contains both classic and type II Cepheids.

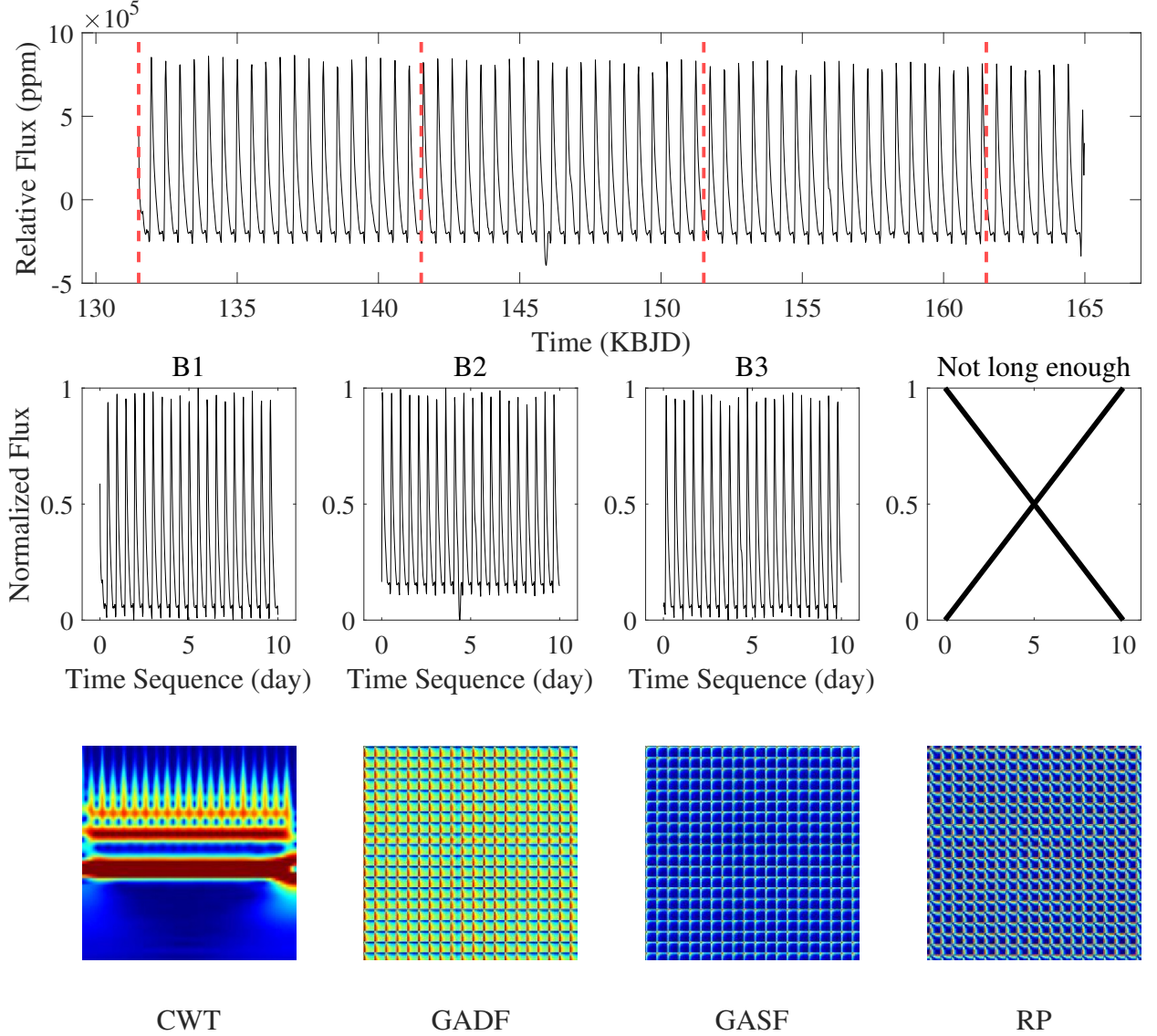


Fig. 1. The transformation from light curves into images. The upper panel shows KIC 7176080 as an example. The middle panels are the partitions divided by the vertical red lines in the upper panel. The bottom panels show the output image of the four transformation methods. The CWT image is from B1. The GAF images are from B2, and the RP image is from B3.

The ϕ is the angle and the r_i is the radius. They are transformed based on the sum of their sine values (GASF) or the difference of their cosine values (GADF). The mapping from the time series to the polar system is injective for the normalized series ($\tilde{x}_i \in [0, 1]$), and the GAFs are $n \times n$ matrixes (Equation

5).

$$\begin{aligned}
 GADF_{ij} &= \sin(\phi_i - \phi_j) \\
 GADF &= \sqrt{I - \tilde{X}^2}^T \cdot \tilde{X} - \tilde{X}^T \cdot \sqrt{I - \tilde{X}^2} \\
 GASF_{ij} &= \cos(\phi_i + \phi_j) \\
 GASF &= \tilde{X}^T \cdot \tilde{X} - \sqrt{I - \tilde{X}^2}^T \cdot \sqrt{I - \tilde{X}^2}
 \end{aligned} \tag{5}$$

Table 2. Sample set

Label	Raw data	Sample object	Training sample
δ Sct	1,337	1,337	111,528
EB	2,821	2,821	226,937
γ Dor	917	917	65,788
HYB	541	541	43,030
RR	1,391	1,373	9,306

Notes. The column raw data shows the number of stars inside the input catalog. The training sample is the final sample set after all pre-processing steps. The second column sample object shows the number of objects in the sample.

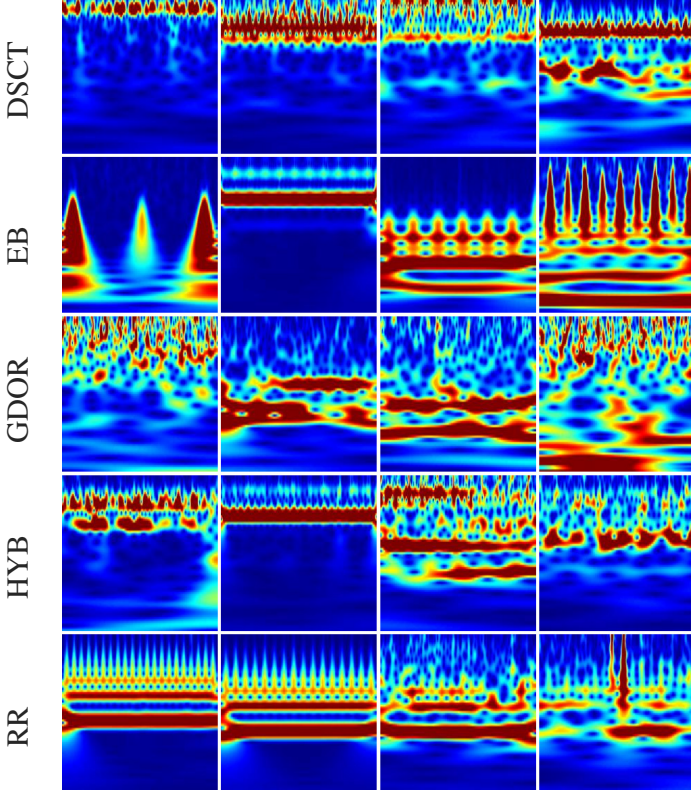


Fig. 2. CWT images from different objects. See more images in Appendix A.

$\tilde{X} = (\tilde{x}_1, \tilde{x}_2, \dots, \tilde{x}_n)$ is a row vector, and the **T** stands for the transpose of the matrix.

3.3. Recurrent Plot

RP is a technique of nonlinear data analysis to visualize a time series or dynamical system. It has been widely applied in many realms. Bradley & Mantilla (2002) found that RP could discover orbits on a chaotic attractor. Mohammadpourfard et al. (2021) compared the RP with GAFs in attack detection of Smart Grid based on CNN algorithms. They concluded that the RP-CNN system had slightly better ($\sim 0.2\%$) recall and F_1 -score than the GAF-CNN system classification. The performances of these two methods are better than Support Vector Machine, k -NN, or random forest. Ahmad et al. (2021) also did several experiments on RP, GAF, and MTF using the CNN scheme to classify electrocardiograms and found that the performance of GAF was similar to RP.

Table 3. Information of origin networks

Model	Stack	Depth	Size (MB)	Para	Input size
VGG-19	16	19	535	144	224×224
GoogLeNet	9	22	27	7.0	224×224
Inception-V3	11	48	89	23.9	299×299
ResNet-101	33	101	167	44.6	224×224
SqueezeNet	8	18	2.64	1.24	227×227
Xception	11	71	85	22.9	299×299

Notes. The stack shows the number of stacks of the models' main idea, for example, Inception module for GoogLeNet and Inception-v3, separable convolution for Xception, fire model for SqueezeNet, residual block for ResNet and 3×3 convolution for VGG. The depth is defined as the largest number of convolution layers and FC layers of a path from input to output. The Para is the number of parameters, and counted in millions.

RP is defined by $R_{i,j} = \Theta(\epsilon - \|x_i - x_j\|)$. x_i, x_j are states at each timings, and $\|\cdot\|$ is a norm. The ϵ is a threshold, and $\Theta(x)$ is the Heaviside function, which equals to 0 if $x < 0$ and equals to 1 otherwise. We use an RP toolbox (Yang 2011; Chen & Yang 2012) to transform the light curves into images.

4. Transfer learning

Deep learning, an advanced technique of machine learning, piles up convolutions, poolings, and FCs, by applying active functions and connections between different layers. The model's output is evaluated with a loss function applied to optimize each parameter in each piled block. The pre-trained CNN models have been proven to be effective in image detection, generation, classification, and regression. We have explored several pre-trained models on the light-curve classification. The parameters in the input, convolution, active, and pooling layers are frozen, while the parameters in FC and output layers are adapted to our classification (Figure 3). The new parameters are trained by the GPUs. The information of our tested networks is shown in Table 3.

4.1. VGG-19

VGG (Simonyan & Zisserman 2015) is a network designed by the Visual Geometry Group from the University of Oxford. The success of VGG has proved that the increased depth could provide better learning accuracy. The VGG-19, a version of VGG net, is constructed with 3×3 convolution layers and 2×2 max-pooling. Unlike earlier architecture, VGG finds that one 5×5 / 7×7 convolution layer can be effectively replaced by two / three 3×3 layers, and significantly decrease the required parameters. However, all VGG nets use three FC layers at the bottom of their architecture, and make the architecture bloated (Szegedy et al. 2015).

Lin et al. 2014 argued that, if global average pooling were applied instead of FC layers, the model would suffer from low overfitting with negligible accuracy variation. Sermanet et al. 2014 found that FC layers could be effectively replaced by 1×1 convolution layers to condense the feature. Both these two methods ended up with a significant decrease in the parameter size. VGG architecture can be reformed in a smaller size in the future. For example, the plain architecture of ResNet (He et al. 2015) is inspired by the VGG net.

We train a VGG-19 net with stochastic gradient descent (SGD) with a momentum 0.9 optimization algorithm, and the

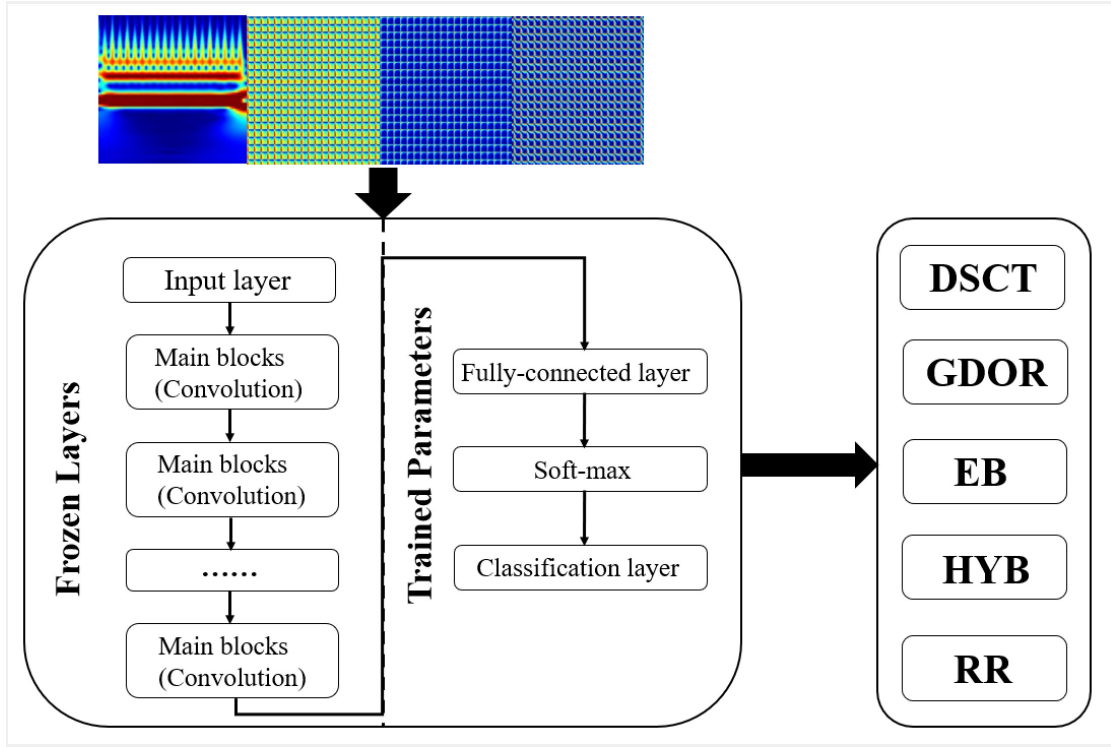


Fig. 3. Summary flowchart of the transfer learning. The parameters in the main blocks are frozen. We train the parameters in the last FC layer and the classification layer. The input images follow the order of CWT, GADF, GASF, and RP.

initial learning rate is 1×10^{-4} . Larger learning rates may fall into, or oscillate between higher local minimums. The last FC and output layers are replaced to adapt our classification.

4.2. GoogLeNet

CNNs apply convolution layers to extract features and connect them by pooling layers in order to detect features and reduce the dimensions. The deeper the architecture, the better result we can obtain. However, deep architecture may cause overfitting, gradient vanishing, and computational inefficiency. The choice of convolution filter size is another difficult, and it still needs to be determined carefully. A big convolution kernel can detect large-scale features, while a small size kernel extracts detailed features. Szegedy et al. (2014) pointed out that the combination of all-size convolution kernels could solve the problem. This came out of the idea of Inception.

GoogLeNet (Szegedy et al. 2014), or Inception-v1, salutes the most classic convolution network LeNet. GoogLeNet proposes the idea of ‘Inception’ to uses the convolution of each kernel size fully and propagates the information in optimization. GoogLeNet won the championship of the ImageNet Large-Scale Visual Recognition Challenge (ILSVRC) 2014.

GoogLeNet also points out a path to constrain training time cost and optimize the distribution of computing resources. The design of the Inception module is based on the stack of 1×1 , 3×3 , 5×5 convolutions, and the pooling process. This inception process contains all convolution information that can be applied to optimization. GoogLeNet replaces the FC layer with the max-pooling layer. The calculation of GoogLeNet is ~ 36 times less than VGG net (Szegedy et al. 2015).

We replace the last two layers of GoogLeNet with a new FC layer and a new classification layer to adapt our classification.

The training strategy uses an SGD with a momentum of 0.9 and an initial learning rate of 1×10^{-4} .

4.3. Inception-v3

Szegedy et al. (2015) made progress in the structure of the Inception module and presented several optimizations in Inception. The evolution of Inception-v3 has four principles. The architecture should avoid sudden compression and representative bottleneck. The network is trained faster when using higher-dimensional representation. The aggressive spatial data are highly correlated without less information loss in the dimensional reduction. The width and depth of a network should increase in balance.

By applying these principles, the Inception module replaces its large convolution filters with smaller ones, and this process can decrease the parameters with similar accuracy. A 5×5 filter can be split into two 3×3 filters, and a 3×3 filter can be reduced into 1×3 and 3×1 filters. Inception has implemented the batch normalization method to restrict calculational cost (Ioffe & Szegedy 2015). The third version of Inception has applied a technique to parallel decrease the scale of feature maps.

We replace the last two layers with a new FC layer and an output layer. The training strategy uses an SGD with a momentum of 0.9 and an initial learning rate of 1×10^{-4} .

4.4. ResNet-101

ResNet (He et al. 2015), the champion of ILSVRC 2015, is the acronym of Residual Net. It is an algorithm based on residual learning. The 101 in the name is the number of layers.

The VGG claimed that the deeper the network, the better the performance, but some experiments found a degenerate problem in deep networks. The degenerate problem (He & Sun 2014) is

that the accuracy reaches the maximum and decreases as the neuron network becomes deeper. This problem is probably caused by gradient vanishing or gradient exploding through the back-propagation. He & Sun (2014) found that the degenerate problem was caused by constructing meaningless identical mappings, which resulted in the optimization difficulty. They presented image learning tests and concluded that a residual net was easy to optimize than the origin network. The ResNet is constructed by several residual blocks and bottleneck blocks. The residual connections transfer the information from shallow layers to deeper layers and solve the problem of gradient vanishing.

We replace the last two layers with a new FC layer and an output layer. The training strategy uses an SGD with a momentum of 0.9 and an initial learning rate of 1×10^{-4} .

4.5. SqueezeNet

SqueezeNet (Iandola et al. 2016) is a small CNN architecture. It can decrease computational costs while keeping a similar accuracy. SqueezeNet decreases the parameter size by using three strategies. The first is replacing 3×3 filters with 1×1 filters, which can straightforwardly reduce the parameters by a factor of nine. The second is decreasing the number of input channels to 3×3 filters. The third strategy is moving downsampling to the bottom of the network. This strategy aims to increase the accuracy by a large activation map. The SqueezeNet architecture stacks ten layers with residual connections, including a 7×7 convolution at the beginning, a 1×1 convolution at the end, and eight fire models. A fire model is designed by a *squeeze* convolution layer connected with an *expand* layer. The *squeeze* layer is constructed with three 1×1 filters to condense the features. The *expand* layer is an inception of four 1×1 filters and four 3×3 filters. See Iandola et al. 2016 for more information.

We replace the last two layers with a new FC layer and an output layer. The training strategy is also an SGD with momentum and learning rate of 0.9 and 1×10^{-4} .

4.6. Xception

The Xception (Chollet 2017) architecture is based on the hypothesis: the mapping of cross-channel correlations and spatial correlations in the feature maps of convolutional neural networks can be entirely decoupled. Xception has a similar parameter size as Inception-v3, while its performance is better on the ImageNet dataset.

We replace the last two layers with a new FC layer and an output layer. The training strategy uses an SGD with a momentum of 0.9 and an initial learning rate of 1×10^{-4} .

5. Result

We apply these pre-trained models to classify the transformed images from light curves and list the accuracies in Table 4. We use different GPUs to complete the calculation. The small models (SqueezeNet and GoogLeNet) are trained with NVIDIA RTX3050, and the other models are trained with NVIDIA RTX3090. All algorithms are trained with a 5% hold-out validation.

5.1. Imaging methods and architectures

The average training accuracies for GADF, GASF, RP, and CWT are 90.1%, 89.4%, 90.8%, and 95.6%, respectively (Table 4).

Table 4. Model size and accuracy

Model	Size (MB)	CWT	GADF	GASF	RP
VGG-19	495.0	97.2%	91.8%	91.4%	92.6%
GoogLeNet	21.2	95.3%	89.5%	88.7%	90.6%
Inception-v3	77.6	94.5%	90.0%	89.4%	89.3%
ResNet-101	151.0	95.7%	90.4%	90.3%	91.8%
SqueezeNet	2.6	96.2%	89.2%	87.5%	90.0%
Xception	74.2	94.5%	89.9%	89.0%	90.3%

Notes. Size and accuracy of all trained models. The column size shows the average model size of all four imaging methods, and the unit is in megabytes. The last four columns, 'CWT', 'GADF', 'GASF', and 'RP', show the accuracy of each imaging method.

CWT has the highest average accuracy among all methods, due to the well-shown feature from full image information. The GAFs and RP output symmetric matrix (images). The result of GAFs and RP is similar to the conclusions in Ahmad et al. (2021) and Mohammadpourfard et al. (2021).

The average training accuracies of each model are similar: 93.25%, 91.03%, 90.80%, 92.05%, 90.73% and 90.93%, following the order of VGG-19, GoogLeNet, Inception-v3, ResNet-101, SqueezeNet and Xception. The VGG net has the best data mining ability, while it has the largest model size. The VGG using the CWT imaging method has the highest classification accuracy (97.2%), while SqueezeNet has 1% lower with a much smaller model size ($\sim 0.5\%$). The SqueezeNet shows good classification accuracy under well-extracted images but a mediocre ability to extract the features from obscure images. The Inception-based models have similar accuracies and similar feature extraction ability. These results show higher accuracy and better prediction performance than traditional methods (e.g., Kim & Bailer-Jones (2016); Christy et al. (2022)).

5.2. Confusion matrix and time performance

The confusion matrices are shown in Appendix B. True positive (TP) is the number that both the target class and the prediction output class are positive. False-positive (FP) is the number that the star belongs to a class but is predicted to other classes, and False negative (FN) is the number that the star does not belong to a class, but is predicted to be in this class. The recall = $\frac{TP}{TP+FN}$, and the precision = $\frac{TP}{TP+FP}$. These two parameters evaluate the ability of prediction.

The recall of HYB is the lowest among different classes. It may be due to the complex construction in which the features of various variable stars are mixed. The FNs of HYB mainly leaks to δ Sct, because δ Sct may dominate the signals. Some δ Scts misclassified as δ Sct/ γ Dor HYB. Balona (2018) claims that nearly all δ Scts are hybrids, and the periodograms show low-frequency peaks, including binarity or rotation. The structure of HYB influences the recalls of δ Sct and γ Dor. The classification result of RR is the best, due to its high purity and data quality.

Deep learning has shown an obvious advantage of computational cost over traditional methods (Kamath et al. 2018; Munir et al. 2019; Lu et al. 2022). We list the prediction time costs in Table 5. GoogLeNet and SqueezeNet have the highest efficiency, while their accuracies are $\sim 2\%$ lower than VGG-19. VGG-19 and ResNet-101 are balance models between the prediction accuracies and time costs.

Table 5. Prediction time cost

Model	CWT	GADF	GASF	RP
VGG-19	25.3	26.0	25.3	25.3
GoogLeNet	5.2	4.9	5.1	4.9
Inception-v3	19.9	19.9	20.5	20.3
ResNet-101	11.5	12.4	11.5	11.6
SqueezeNet	5.0	6.5	5.4	5.9
Xception	40.9	40.9	41.2	41.4

Notes. The prediction time cost of each model. The unit is seconds per 10,000 light curves.

5.3. Blind test

We conducted a blind test using the CWT method on TESS data to assess the generalization ability of our models. TESS utilizes four $2k \times 2k$ CCDs with a 24×24 deg² field of view and 21 arcseconds per pixel to gather information. The observation cadence of TESS is available in two types: 2 minutes and 30 minutes. Light curves obtained from wide-field images captured by TESS are typically undersampled, which could introduce additional noise and even imitate some astrophysical signals of interest, resulting in false positives (Oelkers & Stassun 2018; Bramich 2008; Miller et al. 2008). The light curves are given by Huang et al. 2020, and processed by MIT Quick Look Pipeline (QLP). The low-frequency signals of TESS light curves have been detrended by high pass filters.

The TESS blind test catalog is constructed with Antoci et al. (2019); Forteza et al. (2020); Molnár et al. (2022). Antoci et al. 2019 presents 57 δ Sct, 2 γ Dor, 2 EB and 10 HYB (including 5 δ Sct binaries). Forteza et al. 2020 contains 37 γ Dor and 96 HYB. Molnár et al. 2022 provides 40 RR from its catalog.

Some stars in the blind test catalog are not in standard pulsation mode, showing different or rare performances in their light curves. For example, TIC 30531417, a GDOR that shows unusually strong pulsation amplitude with regular frequency, makes its light curve wide apart from other γ Dor light curves (Lares-Martiz 2022). Some other γ Dor shows obvious eclipsing features, so they are marked as EB. This identification process is done manually. These EBs are easy to recognize, since they show only eclipsing features.

Prior to the blind test, we conducted a cleaning process on the TESS light curves to address contamination by cosmic rays that had not been removed automatically during the TESS data reduction. To accomplish this, we utilized a second-order difference analysis of the light curves, removing affected data points based on a criterion of 2σ , which corresponds to the difference between three continuous data points. Here, σ represents the standard variance of the entire light curve. This process can remove the outliers such as the cosmic ray, without removing other features of the light curves.

In addition, we conducted a thorough review of the light curves and excluded observation sectors exhibiting artificial trends or continuous abnormal signals. These light curves usually show great sunken or 'large mountains' in pattern. As a result of these cleaning procedures, we obtained a final set of 640 light curves from 194 distinct sources, including 51 δ Sct, 18 γ Dor, 17 EB, 38 RR, and 70 HYB. All the manual procedures are done in simple visual scanning. These cleaning processes are realistic for the TESS light curves and other time-sequence data of variable stars.

In accordance with the technique outlined in Section 2.8, we processed the TESS light curves, resulting in 590 samples for prediction. Within the training set, the HYB category primarily consisted of hybrids of δ Sct and γ Dor variables, as well as some binaries with a component exhibiting rotation or pulsation. However, it is worth noting that our HYB training set may not fully capture the feature space of hybrid variables. Consequently, prediction inaccuracies can occur when signal strength ratios differ from those present in the training light curves. It is important to note that such bias arises from the small size of our HYB training sample, rather than the incapability of the deep learning models or the representation disability of the transformation methods. To account for this limitation, we have excluded the HYB class from our blind test. It is clear that additional data and further subtypes are necessary to comprehensively classify HYB variables.

The accuracy results of the blind test can be found in Appendix C, with accuracies of 79.4% for VGG19, 75.8% for GoogLeNet, 78.2% for Inception-v3, 74.2% for ResNet-101, 79.7% for SqueezeNet, and 77.4% for Xception. The VGG19 and SqueezeNet methods demonstrate the best accuracy on the blind test. However, the accuracies below 80% indicate the limited generalization ability of the models, when applied to a different catalog with distinct observation strategy, hardware, and light curve.

The mis-classification observed in our blind test is attributed to the leakage of objects from different classes into the EB class, owing to their nearly constant frequencies and slightly varying amplitudes (see Figure 4). Such a feature is also typical of the γ Dor subtype, such as high amplitude γ Dor, causing confusion between γ Dor and EB. A more effective approach to mitigate this issue is to augment the training set with more samples, such as combining the light curves from both Kepler and TESS.

6. Discussion

Our study proves that deep-learning techniques can lead a revolution in the realm of variable stars, and opens a new path for the future mining of large astronomical data sets. In this section, we would like to discuss some results in transfer learning, blind test, and our future works.

The low generalization ability in the TESS blind test is primarily due to the insufficient training sample size. For instance, Jara-Maldonado et al. 2020 employed 16,451 stars to construct a TESS sample set for detecting exoplanets from light curves. Duev et al. 2019 used over 90,000 images to detect a transient object using CNN in ZTF, while Cui et al. 2021 analyzed more than 140,000 images for transient classification from light curves. Additionally, Aguirre et al. 2018 utilized 246,474 stars from various surveys for variable classification. To improve the generalization ability, we require a larger sample set size.

6.1. Imaging representation ability

We have tested four methods to transform light curves into images, and the representation ability of CWT is better than the other three methods. The performance of machine learning algorithms is correlated with the feature selection (Shalev-Shwartz & Ben-David 2014). CWT presents the time-dependent frequency features that are not included in GAFs or RP.

Based on the Fourier transform, the CWT presents the signal in the time-frequency domain, showing how the light curve varies with time (Percy 2011; Sterken & Jaschek 2005). Its representation ability has been widely accepted. The features in the

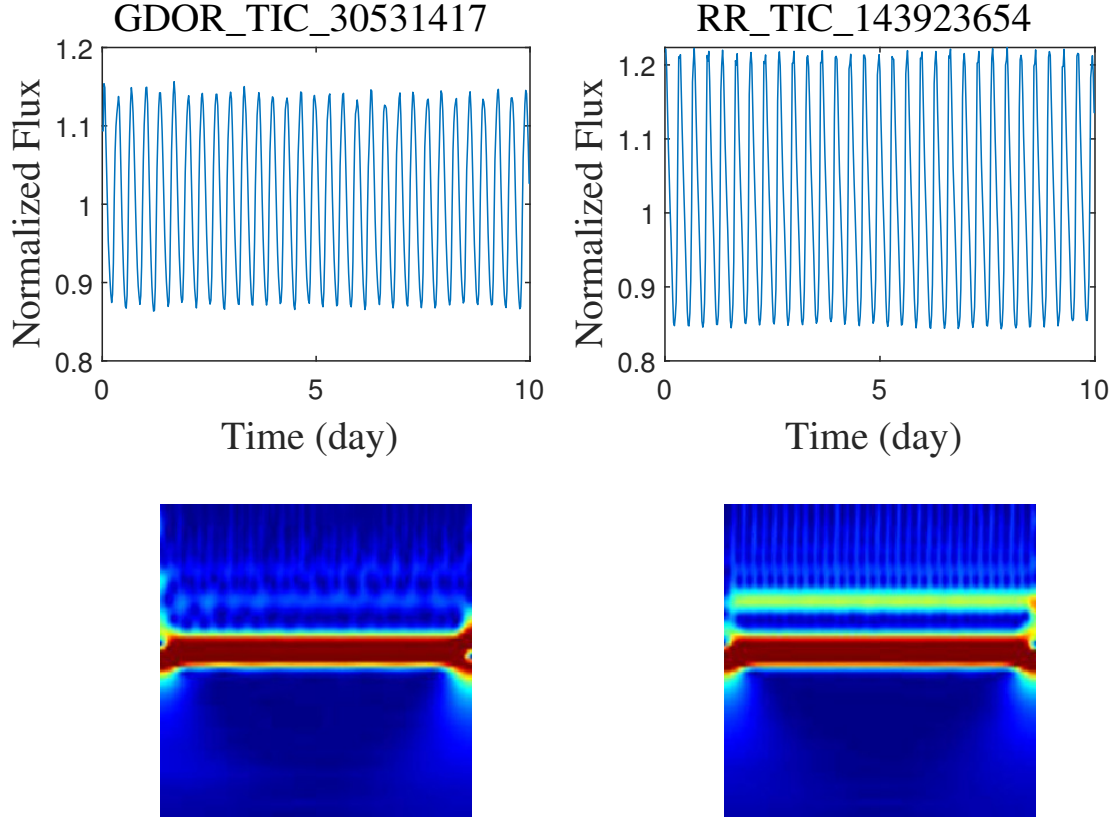


Fig. 4. The light curve and CWT image sample for the EB leaking sources. The top left panel shows the light curve of the first piece of Sector 34 of object TIC 30531417, and the bottom left panel shows its CWT image. The right panel shows the first piece of Sector 28 of object TIC 143923654.

GAFs and RPs are more obscure. GAFs and RP reform have time sequences to a symmetric matrix, and half of the images are redundant. In GAFs and RP, the periods of the light curves are not extracted, while CWT isolates different pulsating modes. Pulsating modes are critical in classification.

6.2. Why transfer learning

Transfer learning is the method that applies the architecture of pre-trained models to a new data set to reduce computational costs. A fine-tuning pre-trained model with transfer learning is much faster than training a network with randomly initialized weights and biases. To show the advantage of transfer learning, we construct a simple CNN model (ICRFDS) and test its classification accuracy.

The ICRFDS is constructed by the sequential connection of an input layer, three convolution blocks, a RELU layer, an FC layer, a dropout layer, and a softmax layer. The convolution block is constructed by twenty 3×3 convolution filters with stride 1 and no padding connected to a 2×2 max-pooling with stride 1 and same padding. The output then flows to a batch normalization layer. The ICRFDS architecture has a model size of 17.8 MB, similar to GoogLeNet, and presents a total accuracy of 84.6% for CWT images with the same training strategy. Compared to 95.6%, the average of CWT, the advantage of transfer learning is obvious in our classification.

6.3. Future work

6.3.1. Phase dependent importance

The variation in stellar photometry carries both the period and the phase information. The phase has the information about the pulsation stage of the star (Percy 2011). The phase of EB tells the spatial relationship of the binary. The phase of rotation variables shows the position of the flare or stellar spot on the surface. Different phase plays different roles in the classification. We will investigate phase-dependent importance in our future work. This investigation may help us achieve a precise, quick classification for short cadence light curves.

6.3.2. Transformer

Vaswani et al. (2017) presents a new scheme for Natural Language Processing problem aiming at Google Neural Machine Translation (NLP)³. The authors present the model, transformer, constructed with encoders and decoders, and uses self-attention as the main mechanism. The encoder block is constructed with a stack of 6 encoder blocks, while the decoders are constructed with the same amount of decoder blocks. Each encoder is connected to the decoder. The encoder contains a multi-head self-attention mechanism and a fully connected feed-forward network. There are residual connections inside the encoder and decoder block. The decoder contains one more self-attention mechanism that allows information to transfer from behind.

The transformer, applying weights and fully connected layers to construct its attention mechanism, opens a new gate to the

³ The descriptions refer to Alammari, J (2018).

NLP problem. It has been applied to image processing. Huang et al. (2019a) has developed an Attention on Attention (AoA) scheme to caption the images (giving linguistic descriptions to an image), and gain better results than other algorithms, including Long Short Time Memory (LSTM). Fu et al. (2019) construct a Dual Attention Network to deal with the scene segmentation (such as a picture of a cityscape, finding each pixel belongs to the road, the car, or a tree) problem and win the highest score among other deep-learning algorithms. Huang et al. (2019b) applies attention in a criss-cross network, and gains a comparable result as Fu et al. (2019), better than other architectures without attention.

Applying attention to time series has an advantage; time series can be the input of attention modular straightforwardly. The imaging time series process is not necessary. This could avoid the error and distortion caused by the combination of pixels, and other transformation processes.

6.3.3. Yansong Scheme

Yansong Scheme (Li & Han 2022) is an algorithm including both model-based and model-free parts (Qu et al. 2020). This scheme introduced a model-free part (model-free fitting, which can be machine learning, deep learning, or transfer learning algorithms) in order to solve model-based problems. Model-based algorithms require less data than model-free algorithms (Tu & Recht 2019).

We sometime couldn't have enough samples for rare variable objects. Yansong Scheme can be applied to train unbalanced samples. Applying the Yansong Scheme and physical model may lead to a better prediction of the infertile data than traditional methods.

6.3.4. SiTian Application

The SiTian (Liu et al. 2021) prototype, mini-SiTian, is now ongoing⁴, and will generate its internal data release. SiTian requires a methodology with a balance of both prediction time cost and accuracy. Data from SiTian will include three-band information. We will apply numerical simulations to construct SiTian light curves and further test light curve classification with deep learning. Due to the 40GB per minute of data produced by SiTian, we also need to find a trade-off between model accuracy and the time cost of both training and prediction.

The mini-SiTian is now generating low-resolution photometry, allowing us to generate mock data from ground-based surveys. The result of this work has shown the feasibility of transfer learning to construct the early pipeline of mini-SiTian. New transfer learning models will be trained by providing the mock catalog, but not the models trained by *Kepler* observations. VGG net or SqueezeNet will have the top priority. The models will be evaluated and form the early pipeline until SiTian produces more data for a from-scratch training.

Acknowledgements. This work was supported by the National Programs on Key Research and Development Project (grant No.2019YFA0405504 and 2019YFA0405000) and the National Natural Science Foundation of China (NSFC) through grants NSFC-11988101/11973054/11933004. Strategic Priority Program of the Chinese Academy of Sciences under grant number XDB41000000. We acknowledge the science research grants from the China Manned Space Project with NO.CMS-CSST-2021-B07. JFL acknowledges support from the New Cornerstone Science Foundation through the NewCornerstone Investigator Program and the XPLOER PRIZE. The paper includes data col-

lected by the Kepler mission. Funding for the Kepler mission is provided by the NASA Science Mission Directorate. All of the data presented in this paper were obtained from the Mikulski Archive for Space Telescopes (MAST). STScI is operated by the Association of Universities for Research in Astronomy, Inc., under NASA contract NAS5-26555. Support for MAST for non-HST data is provided by the NASA Office of Space Science via grant NNX09AF08G and by other grants and contracts.

References

- Abdul-Masih, M., Prša, A., Conroy, K., et al. 2016, *The Astronomical Journal*, 151, 101
- Aguirre, C., Pichara, K., & Becker, I. 2018, *Monthly Notices of the Royal Astronomical Society*, 482, 5078
- Ahmad, Z., Tabassum, A., Guan, L., & Khan, N. 2021, *ECG Heartbeat Classification Using Multimodal Fusion*
- Antoci, V., Cunha, M. S., Bowman, D. M., et al. 2019, *Monthly Notices of the Royal Astronomical Society*, 490, 4040
- Arjona, R. & Nesseris, S. 2020, *Physical Review D*, 101, 123525
- Artyukhina, N., Durlevich, O., Frolov, M., et al. 1995
- Bai, Y., Yang, J., Wang, J., & Li, Q. 2020, *IEEE Access*, 8, 105118
- Balona, L. A. 2018, *Monthly Notices of the Royal Astronomical Society*, 479, 183
- Barchi, P., de Carvalho, R., Rosa, R., et al. 2020, *Astronomy and Computing*, 30, 100334
- Bellm, E. 2014, in *The Third Hot-wiring the Transient Universe Workshop*, ed. P. R. Wozniak, M. J. Graham, A. A. Mahabal, & R. Seaman, 27–33
- Bertin, E. & Arnouts, S. 1996, *A&AS*, 117, 393
- Borucki, W. J., Koch, D., Basri, G., et al. 2010, *Science*, 327, 977
- Bradley, E. & Mantilla, R. 2002, *Chaos: An Interdisciplinary Journal of Nonlinear Science*, 12, 596
- Bradley, P. A., Guzik, J. A., Miles, L. F., et al. 2015, *AJ*, 149, 68
- Bramich, D. M. 2008, *MNRAS*, 386, L77
- Chen, Y., Keogh, E., Hu, B., et al. 2015, *The UCR Time Series Classification Archive*, www.cs.ucr.edu/~eamonn/time_series_data/
- Chen, Y. & Yang, H. 2012, *Chaos, Solitons and Fractals*, 45, 978, copyright: Copyright 2012 Elsevier B.V., All rights reserved.
- Chollet, F. 2017, *Xception: Deep Learning with Depthwise Separable Convolutions*
- Christy, C. T., Jayasinghe, T., Stanek, K. Z., et al. 2022, *Publications of the Astronomical Society of the Pacific*, 134, 024201
- Conroy, K. E., Prša, A., Stassun, K. G., et al. 2014a, *Publications of the Astronomical Society of the Pacific*, 126, 914–922
- Conroy, K. E., Prša, A., Stassun, K. G., et al. 2014b, *The Astronomical Journal*, 147, 45
- Cortes, C. & Vapnik, V. 1995, *Machine Learning*, 20, 273
- Cover, T. & Hart, P. 1967, *IEEE Trans. Inf. Theory*, 13, 21
- Cui, K., Liu, J., Feng, F., & Liu, J. 2021, *The Astronomical Journal*, 163, 23
- Deb, S. & Singh, H. P. 2009, *A&A*, 507, 1729
- Duev, D. A., Mahabal, A., Ye, Q., et al. 2019, *MNRAS*, 486, 4158
- Dupret, M.-A., Grigahcène, A., Garrido, R., et al. 2005, *Monthly Notices of the Royal Astronomical Society*, 361, 476
- Dupret, M.-A., Grigahcène, A., Garrido, R., Gabriel, M., & Scuflaire, R. 2004, *A&A*, 414, L17
- Durlevich, O., Frolov, M., Kazarovets, E., & Samus, N. 1994
- Eddington, A. 1917, *The Observatory*, 40, 290
- Forteza, S. B., Moya, A., Barrado, D., et al. 2020, *Astronomy & Astrophysics*, 638, A59
- Fu, J., Liu, J., Tian, H., et al. 2019, in *Proceedings of the IEEE/CVF Conference on Computer Vision and Pattern Recognition (CVPR)*
- Galarza, C. A., Daflon, S., Placco, V. M., et al. 2022, *A&A*, 657, A35
- Han, H.-G., Cui, K.-M., Liu, J.-F., et al. 2021, *Research in Astronomy and Astrophysics*, 21, 142
- He, K. & Sun, J. 2014, *Convolutional Neural Networks at Constrained Time Cost*
- He, K., Zhang, X., Ren, S., & Sun, J. 2015, *Deep Residual Learning for Image Recognition*
- Hinners, T. A., Tat, K., & Thorp, R. 2018, *The Astronomical Journal*, 156, 7
- Huang, C. X., Vanderburg, A., Pál, A., et al. 2020, *Research Notes of the AAS*, 4, 204
- Huang, L., Wang, W., Chen, J., & Wei, X.-Y. 2019a, in *Proceedings of the IEEE/CVF International Conference on Computer Vision (ICCV)*
- Huang, Z., Wang, X., Huang, L., et al. 2019b, in *Proceedings of the IEEE/CVF International Conference on Computer Vision (ICCV)*
- Iandola, F. N., Han, S., Moskewicz, M. W., et al. 2016, *arXiv e-prints*, arXiv:1602.07360
- Ioffe, S. & Szegedy, C. 2015, *Batch Normalization: Accelerating Deep Network Training by Reducing Internal Covariate Shift*

⁴ https://njb.cas.cn/kydt2016/zdtp/202111/t20211110_6248024.html

- Jara-Maldonado, M., Alarcon-Aquino, V., Rosas-Romero, R., Starostenko, O., & Ramirez-Cortes, J. M. 2020, *Earth Science Informatics*, 13, 573
- Kamath, C. N., Bukhari, S. S., & Dengel, A. 2018, in *Proceedings of the ACM Symposium on Document Engineering 2018, DocEng '18* (New York, NY, USA: Association for Computing Machinery)
- Kholopov, P., Samus, N., Frolov, M., et al. 1988
- Kim, D.-W. & Bailer-Jones, C. A. L. 2016, *A&A*, 587, A18
- Kirk, B., Conroy, K., Prša, A., et al. 2016, *The Astronomical Journal*, 151, 68
- LaCourse, D. M., Jek, K. J., Jacobs, T. L., et al. 2015, *Kepler Eclipsing Binary Stars. VI. Identification of Eclipsing Binaries in the K2 Campaign 0 Data-set*
- Lares-Martiz, M. 2022, *Frontiers in Astronomy and Space Sciences*, 9
- LeCun, Y., Bengio, Y., et al. 1995, *The handbook of brain theory and neural networks*, 3361, 1995
- LeCun, Y., Bottou, L., Bengio, Y., & Haffner, P. 1998, *Proceedings of the IEEE*, 86, 2278
- LeCun, Y. et al. 2015, URL: <http://yann.lecun.com/exdb/lenet>, 20, 14
- Li, Y. & Han, S. 2022, *Accelerating Model-Free Policy Optimization Using Model-Based Gradient: A Composite Optimization Perspective*
- Lilly, J. M. & Olhede, S. C. 2008, *IEEE Transactions on Signal Processing*, 57, 146
- Lilly, J. M. & Olhede, S. C. 2010, *IEEE transactions on information theory*, 56, 4135
- Lilly, J. M. & Olhede, S. C. 2012, *IEEE Transactions on Signal Processing*, 60, 6036
- Lin, M., Chen, Q., & Yan, S. 2014, *Network In Network*
- Liu, J., Soria, R., Wu, X.-F., Wu, H., & Shang, Z. 2021, *An. Acad. Bras. Ciênc.* vol.93 supl.1, 93, 20200628
- Lu, H., Ehwerhemuepha, L., & Rakovski, C. 2022, *BMC Medical Research Methodology*, 22, 181
- Mahabal, A., Rebbapragada, U., Walters, R., et al. 2019, *PASP*, 131, 038002
- Maschi, F. J., Laher, R. R., Rusholme, B., et al. 2018, *Publications of the Astronomical Society of the Pacific*, 131, 018003
- Matijević, G., Prša, A., Orosz, J. A., et al. 2012, *The Astronomical Journal*, 143, 123
- Miller, J. P., Pennypacker, C. R., & White, G. L. 2008, *Publications of the Astronomical Society of the Pacific*, 120, 449
- Mohammadpourfard, M., Genc, I., Lakshminarayana, S., & Konstantinou, C. 2021, in *2021 IEEE International Conference on Communications, Control, and Computing Technologies for Smart Grids (SmartGridComm)*, 121–126
- Molnár, L., Bódi, A., Pál, A., et al. 2022, *ApJS*, 258, 8
- Molnar, L., Plachy, E., Juhasz, A. L., & Rimoldini, L. 2018, *Astronomy & Astrophysics*, 620, A127
- Munir, M., Chattha, M. A., Dengel, A., & Ahmed, S. 2019, in *2019 18th IEEE International Conference On Machine Learning And Applications (ICMLA)*, 561–566
- Ngiam, J., Chen, Z., Chia, D., et al. 2010, in *Advances in Neural Information Processing Systems*, ed. J. Lafferty, C. Williams, J. Shawe-Taylor, R. Zemel, & A. Culotta, Vol. 23 (Curran Associates, Inc.)
- Oelkers, R. J. & Stassun, K. G. 2018, *AJ*, 156, 132
- Olhede, S. C. & Walden, A. T. 2002, *IEEE Transactions on Signal Processing*, 50, 2661
- Pan, S. J. & Yang, Q. 2010, *IEEE Transactions on Knowledge and Data Engineering*, 22, 1345
- Percy, J. R. 2011, Cambridge University Press
- Pierce, M. J., Welch, D. L., McClure, R. D., et al. 1994, *Nature*, 371, 385
- Prša, A., Batalha, N., Slawson, R. W., et al. 2011, *The Astronomical Journal*, 141, 83
- Qu, G., Yu, C., Low, S., & Wierman, A. 2020, *Combining Model-Based and Model-Free Methods for Nonlinear Control: A Provably Convergent Policy Gradient Approach*
- Quinlan, J. R. 1986, *Machine Learning*, 1, 81
- Sadoun, L. 2018, *Time Series Analysis-Data, Methods, and Applications*, 1
- Samus, N. N., Pastukhova, E. N., Durlevich, O. V., Kazarovets, E. V., & Kireeva, N. 2021, *Peremennye Zvezdy*, 41, 7
- Sanchez Arias, J. P., Corsico, A. H., & Althaus, L. G. 2017, *A&A*, 597, A29
- Schutter, A. & Shamir, L. 2015, *Astronomy and Computing*, 12, 60
- Sermanet, P., Eigen, D., Zhang, X., et al. 2014, *OverFeat: Integrated Recognition, Localization and Detection using Convolutional Networks*
- Shalev-Shwartz, S. & Ben-David, S. 2014, *Understanding Machine Learning: From Theory to Algorithms* (Cambridge University Press)
- Simonyan, K. & Zisserman, A. 2015, *Very Deep Convolutional Networks for Large-Scale Image Recognition*
- Slawson, R. W., Prša, A., Welsh, W. F., et al. 2011, *The Astronomical Journal*, 142, 160
- Sterken, C. & Jaschek, C. 2005, *Light Curves of Variable Stars*
- Stetson, P. B. 1996, *Publications of the Astronomical Society of the Pacific*, 108, 851
- Stone, C. J. 1977, *The Annals of Statistics*, 5, 595
- Szegedy, C., Liu, W., Jia, Y., et al. 2014, *Going Deeper with Convolutions*
- Szegedy, C., Vanhoucke, V., Ioffe, S., Shlens, J., & Wojna, Z. 2015, *Rethinking the Inception Architecture for Computer Vision*
- Tang, W., Long, G., Liu, L., et al. 2020, *Rethinking 1D-CNN for Time Series Classification: A Stronger Baseline*
- Tu, S. & Recht, B. 2019, *The Gap Between Model-Based and Model-Free Methods on the Linear Quadratic Regulator: An Asymptotic Viewpoint*
- Van Cleve, J. E. & Caldwell, D. A. 2016, *Kepler Instrument Handbook*, Tech. rep.
- Vaswani, A., Shazeer, N., Parmar, N., et al. 2017, *Attention Is All You Need*
- Wang, C., Bai, Y., López-Sanjuan, C., et al. 2022, *A & A*, 659, A144
- Wang, Z. & Oates, T. 2015, *Imaging Time-Series to Improve Classification and Imputation*
- Xiong, D., Deng, L., & Zhang, C. 2015, *Monthly Notices of the Royal Astronomical Society*, 451, 3354
- Xiong, D. R., Deng, L., Zhang, C., & Wang, K. 2016, *MNRAS*, 457, 3163
- Yang, H. 2011, *IEEE Transactions on Biomedical Engineering*, 58, 339
- Yang, H. & Liu, J. 2019, *ApJS*, 241, 29
- Yang, L., Yuan, H., Xiang, M., et al. 2021, *arXiv e-prints*, arXiv:2112.07304
- Zhang, G., Si, Y., Wang, D., Yang, W., & Sun, Y. 2019, *IEEE Access*, 7, 171570
- Zhao, B., Lu, H., Chen, S., Liu, J., & Wu, D. 2017, *Journal of Systems Engineering and Electronics*, 28, 162

Table A.1. Sample of light curves

Label	Column 1	Column 2	Column 3	Column 4
δ Sct	1162150	1294670	1571717	1576115
EB	1026032	1433410	1433980	1575690
γ Dor	1161908	1432149	1872262	2975214
HYB	1431794	1573174	9971786	2860851
RR	3866709	7021124	217974025	229134937

Notes. The KIC of light curves in Figure 2 to Figure A.3. The last two RRs are from *K2* catalog.

Appendix A: Light curves

Figure 2, A.1, A.2, and A.3 present the transformed images from different methods in Section 3. All figures follow the order of δ Sct, EB, γ Dor, HYB, from top to bottom. Each column shows the same object, and their KICs are listed in Table A.1. We also present the light curves of these samples in Figure A.4 to A.8. The pre-processing of these light curves are shown in Section 2.8. Each light curve is a quarter in *Kepler* observation, and the area between the red lines is the partition shown in Figure 2, A.1, A.2, and A.3.

Appendix B: Confusion matrix

We present all confusion matrices here. The different grayscale of the confusion matrix shows the number and fraction of each class. The bottom brightest blocks are the recall (fractions with larger font size) of each corresponding label, and the smaller percentage is $(1 - recall)$. The right brightest blocks are each class's precision (larger font size), and the smaller ones are $(1 - precision)$. The bottom right block shows the total accuracy (larger font size) and the error rate (the smaller one). The complete figure set (24 images) is available in the online journal.

Appendix C: Blind test confusion matrix

We show the blind test confusion matrices here. The different grayscale of the confusion matrix shows the number and fraction of each class. The bottom brightest blocks are the recall (fractions with larger font size) of each corresponding label, and the smaller percentage is $(1 - recall)$. The right brightest blocks are each class's precision (larger font size), and the smaller ones are $(1 - precision)$. The bottom right block shows the total accuracy (larger font size) and the error rate (the smaller one). The complete figure set (6 images) is available in the online journal.

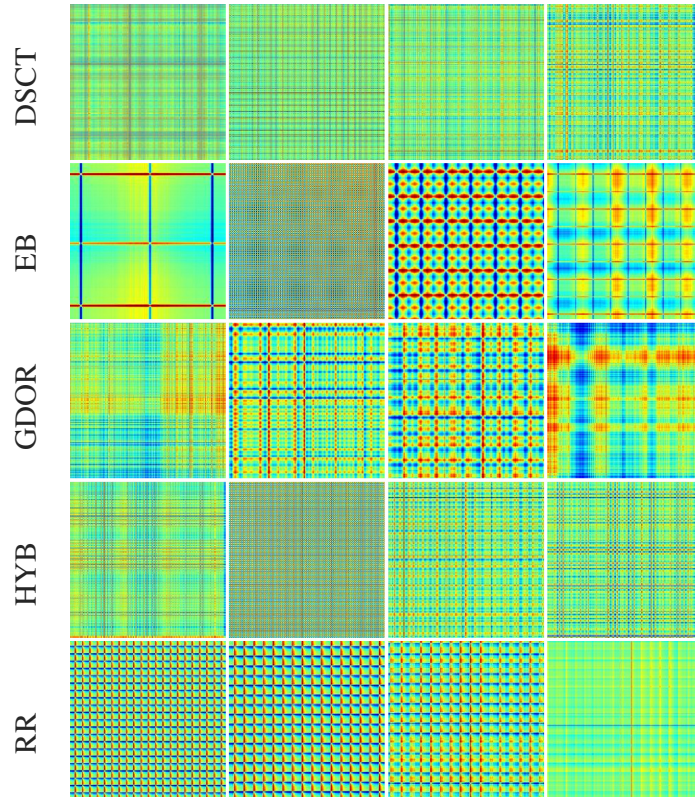


Fig. A.1. GADF images. Each object in this figure are the same as the object in Figure 2.

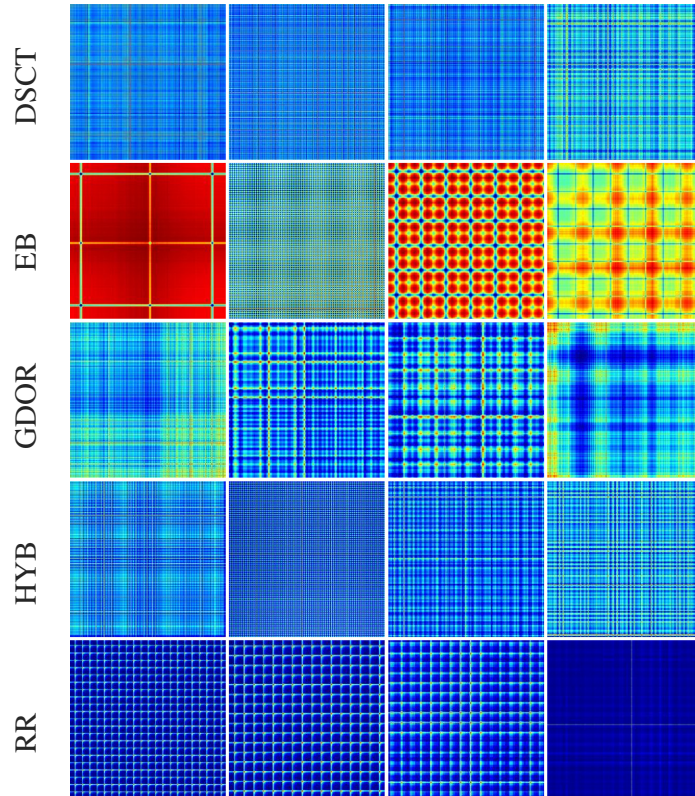


Fig. A.2. GASF images. Each object in this figure are the same as the object in Figure 2.

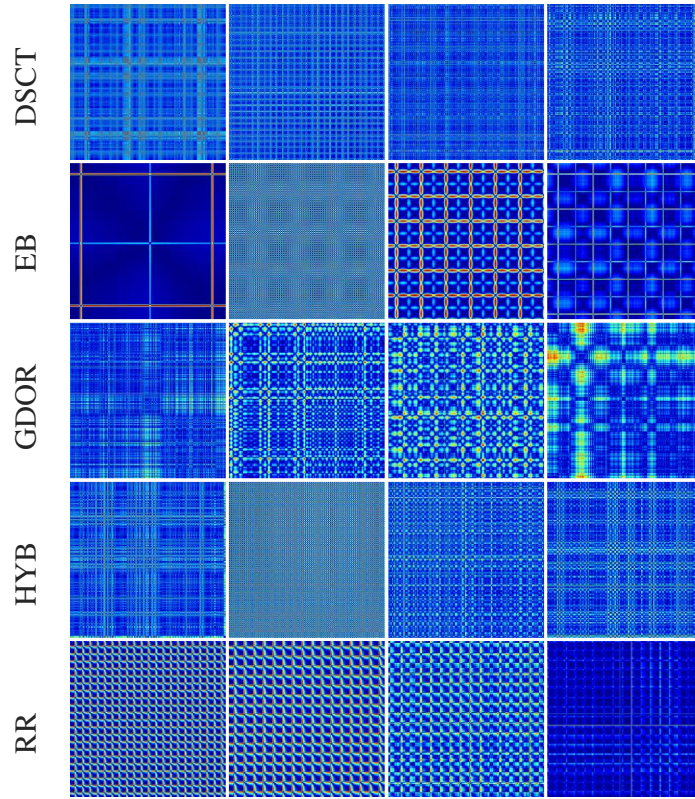


Fig. A.3. RP images. Each object in this figure are the same as the object in Figure 2.

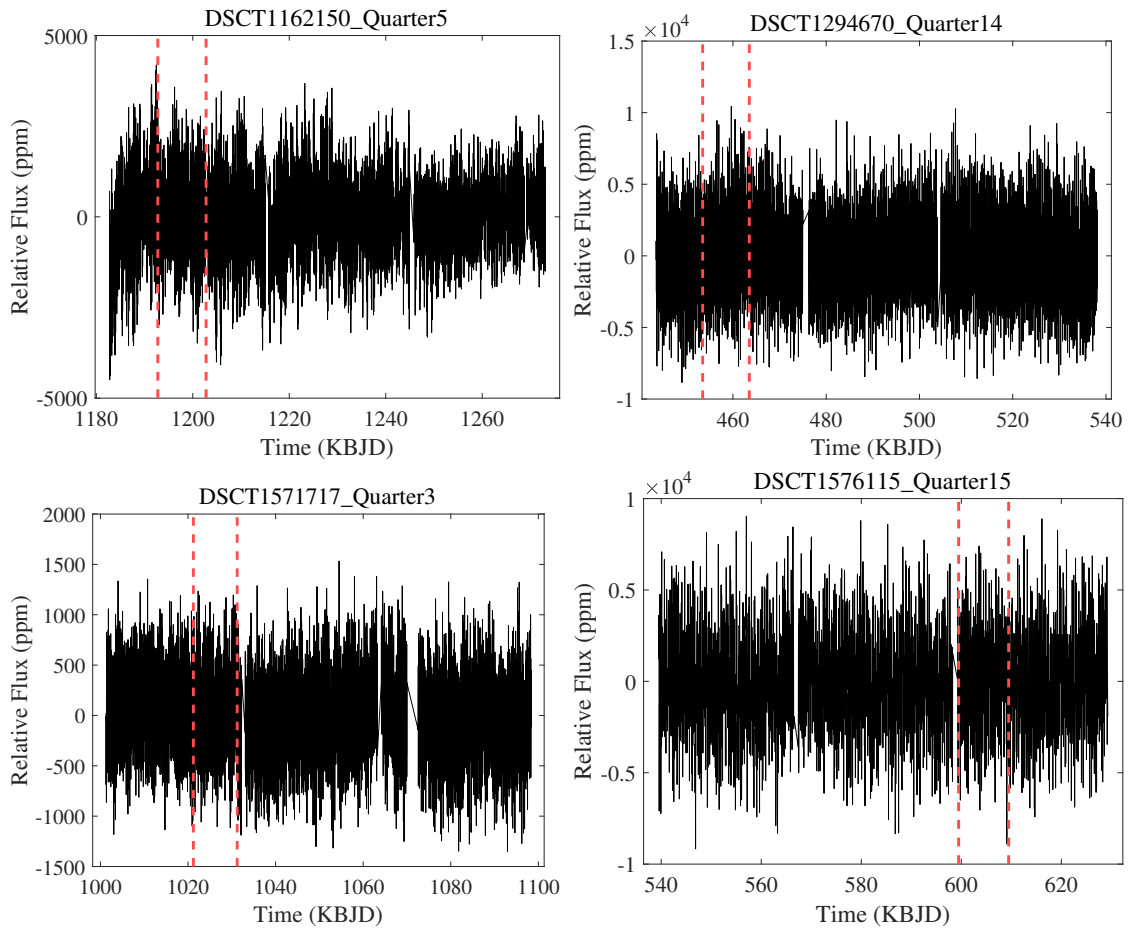


Fig. A.4. The DSCT light curves. The red line stands for the interval shown in Figure 2 to Figure A.3.

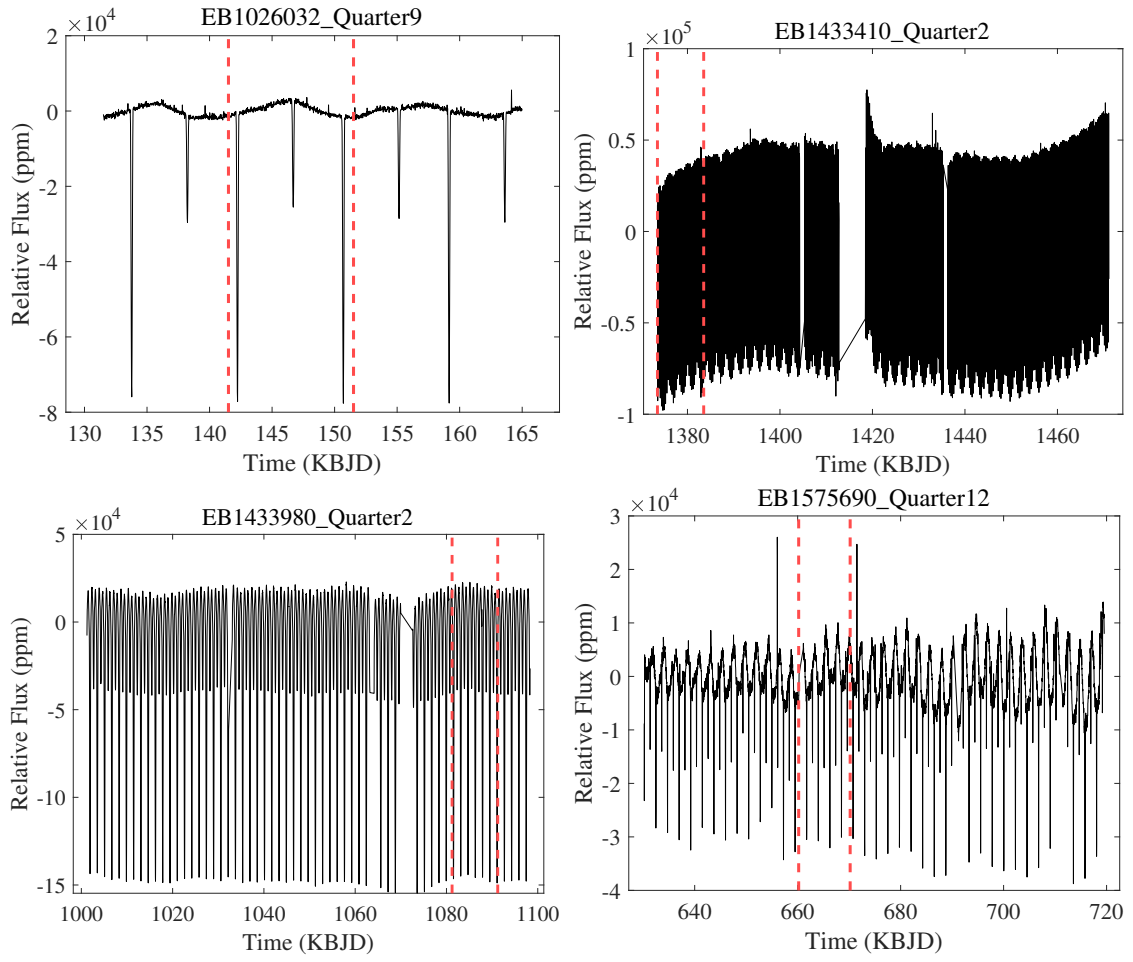


Fig. A.5. The EB light curves. The red line stands for the interval Figure 2 to Figure A.3.

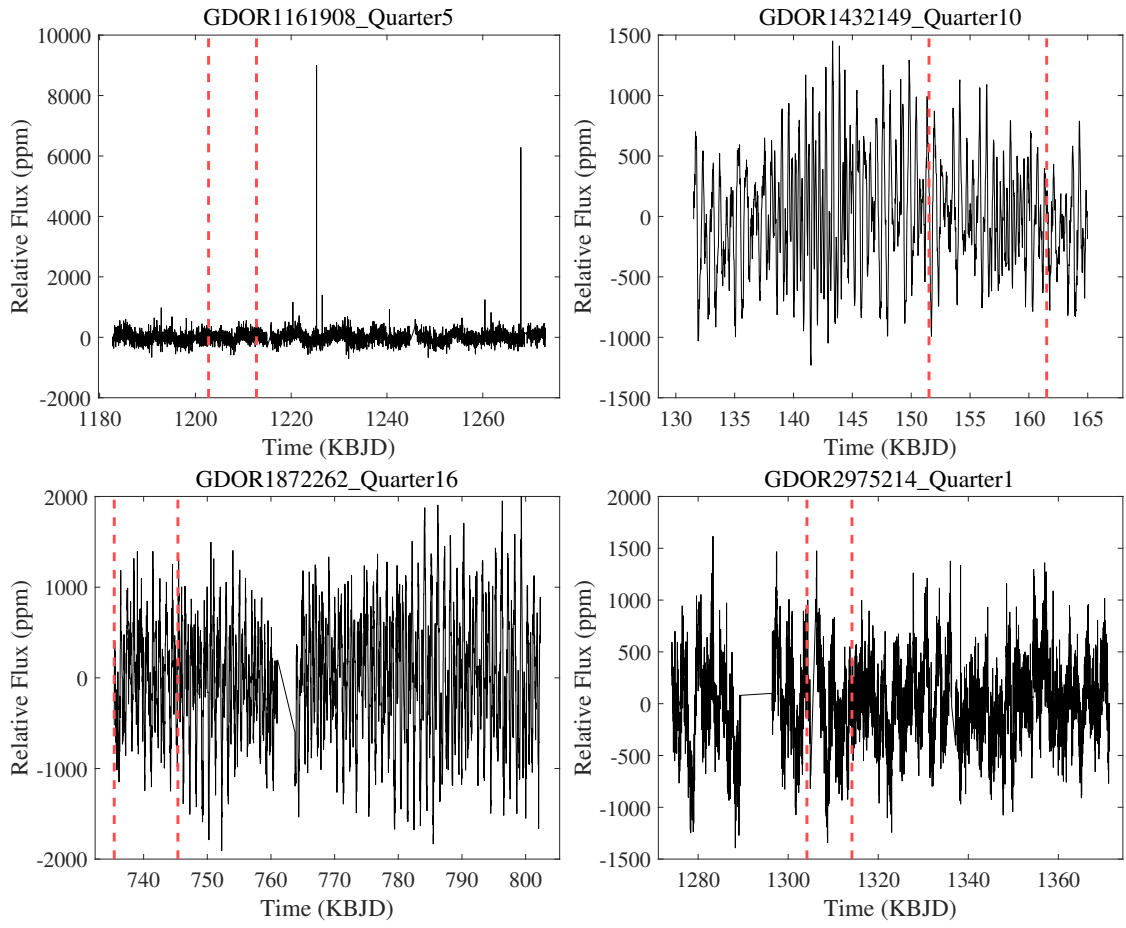


Fig. A.6. The GDor light curves. The red line stands for the interval Figure 2 to Figure A.3.

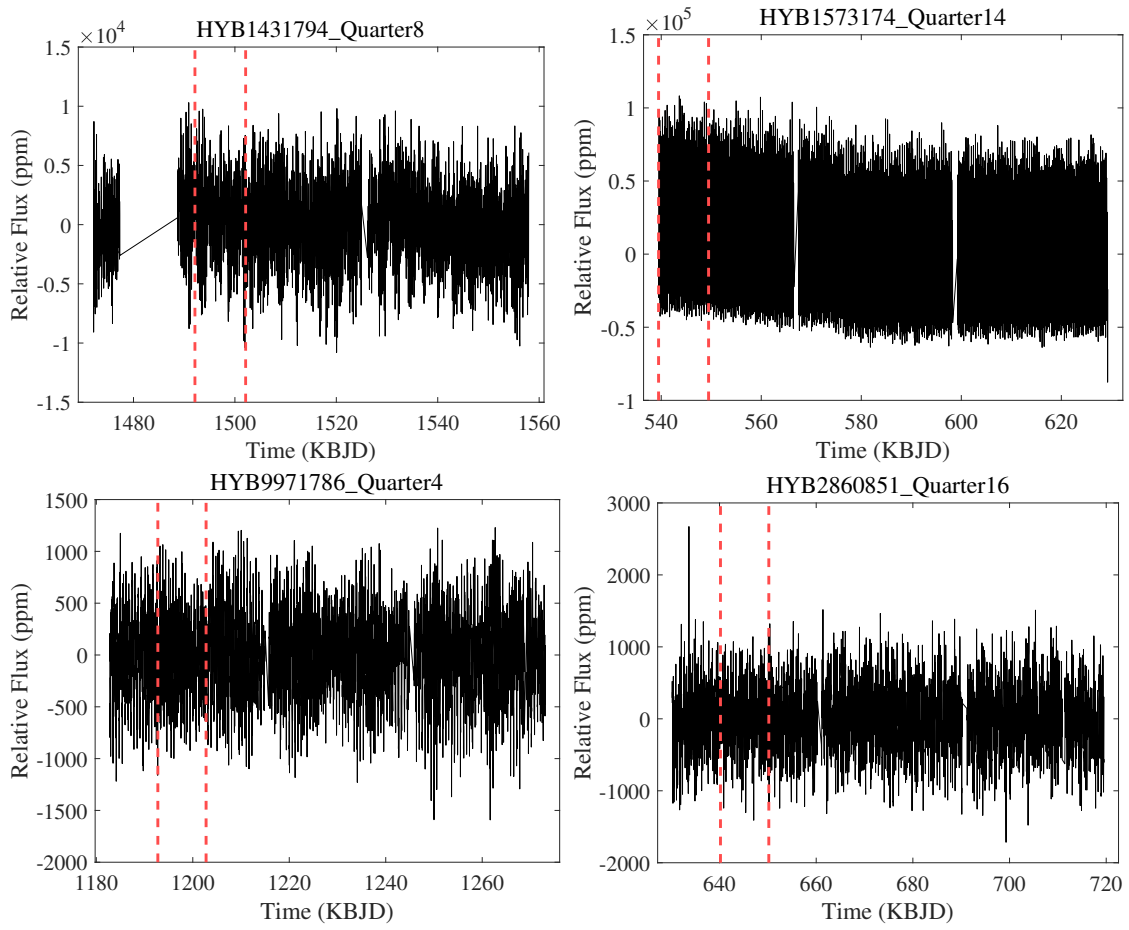


Fig. A.7. The HYB light curves. The red line stands for the interval Figure 2 to Figure A.3.

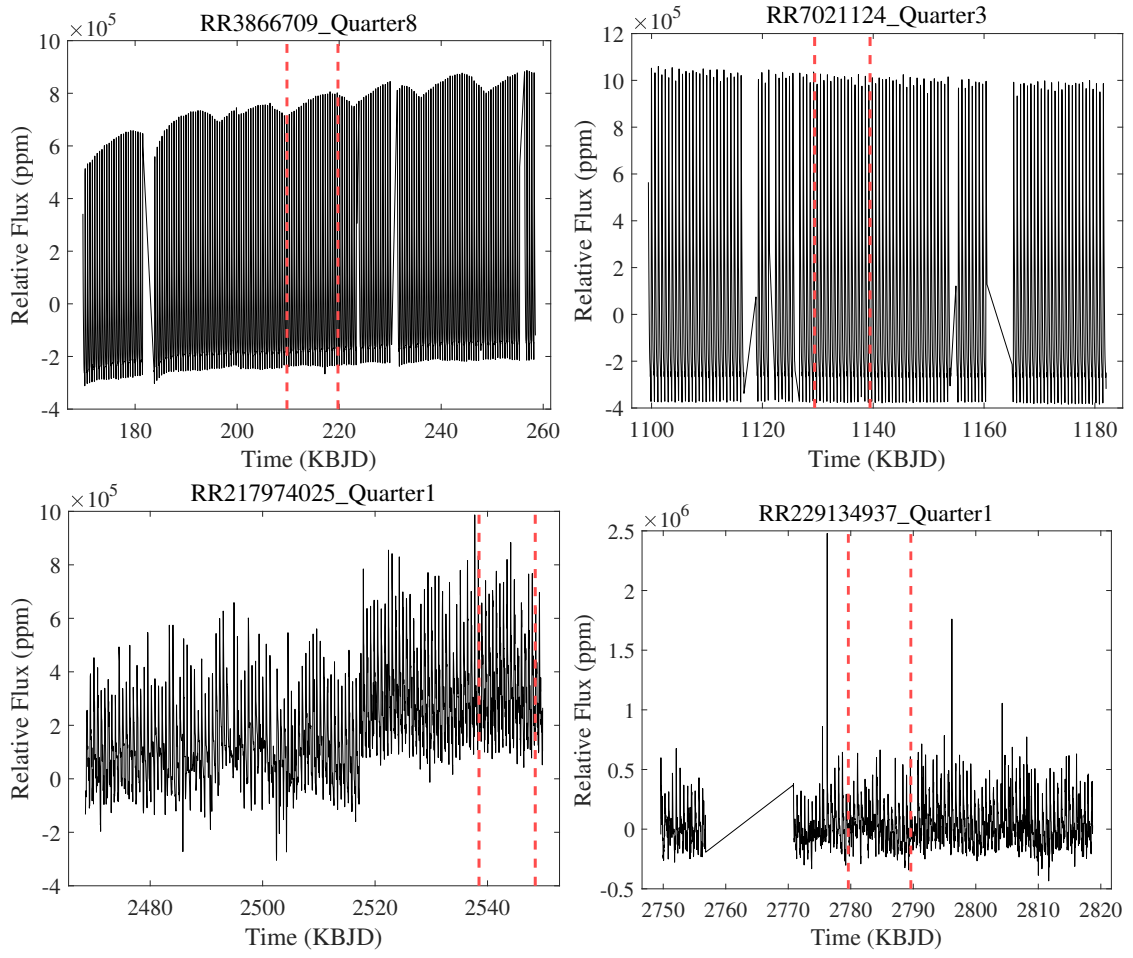


Fig. A.8. The RR light curves. The red line stands for the interval Figure 2 to Figure A.3.

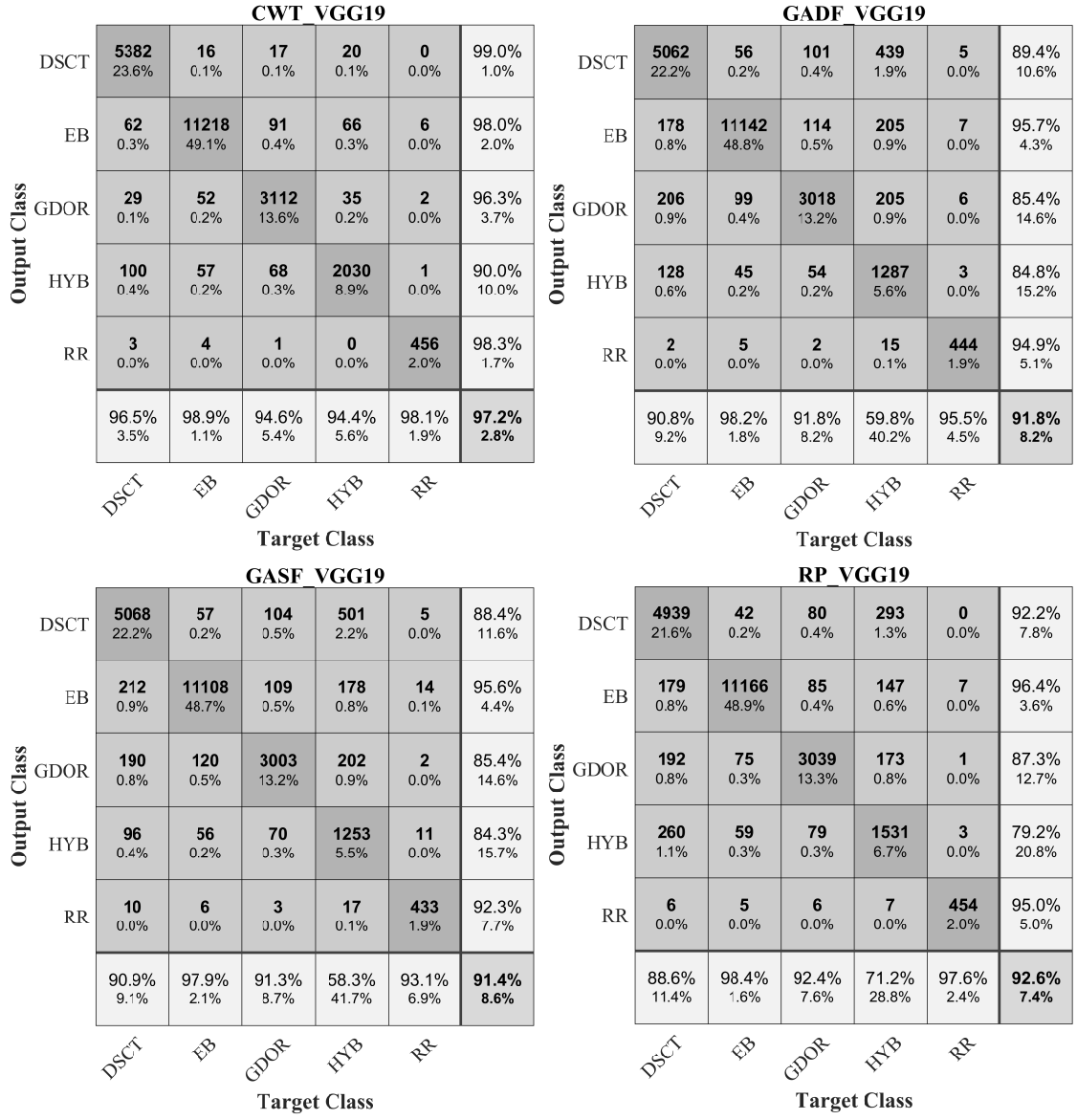


Fig. B.1. The confusion matrixes for VGG19 architecture.

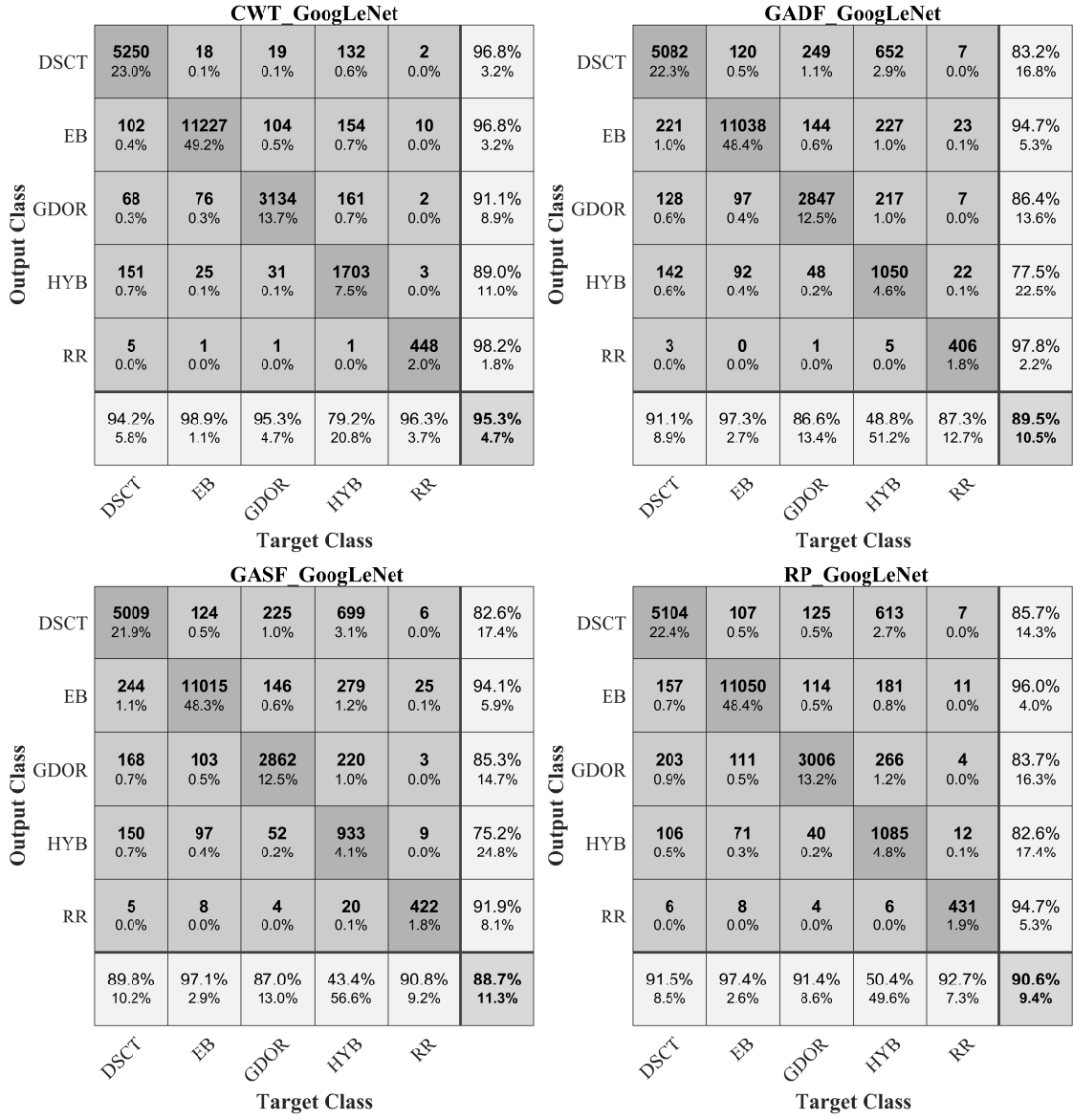


Fig. B.2. The confusion matrixes for GoogLeNet architecture.

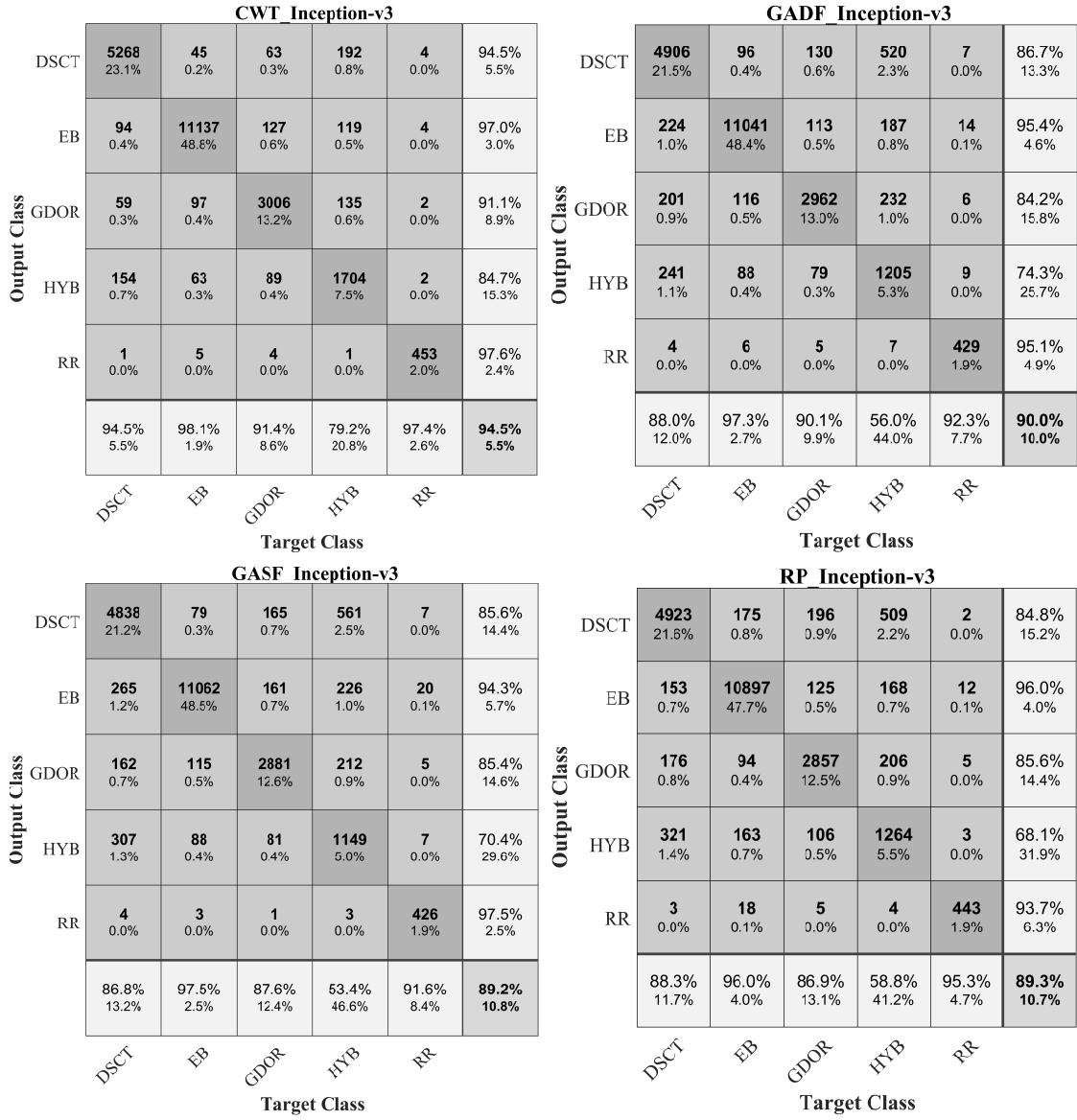


Fig. B.3. The confusion matrixes for Inception-v3 architecture.

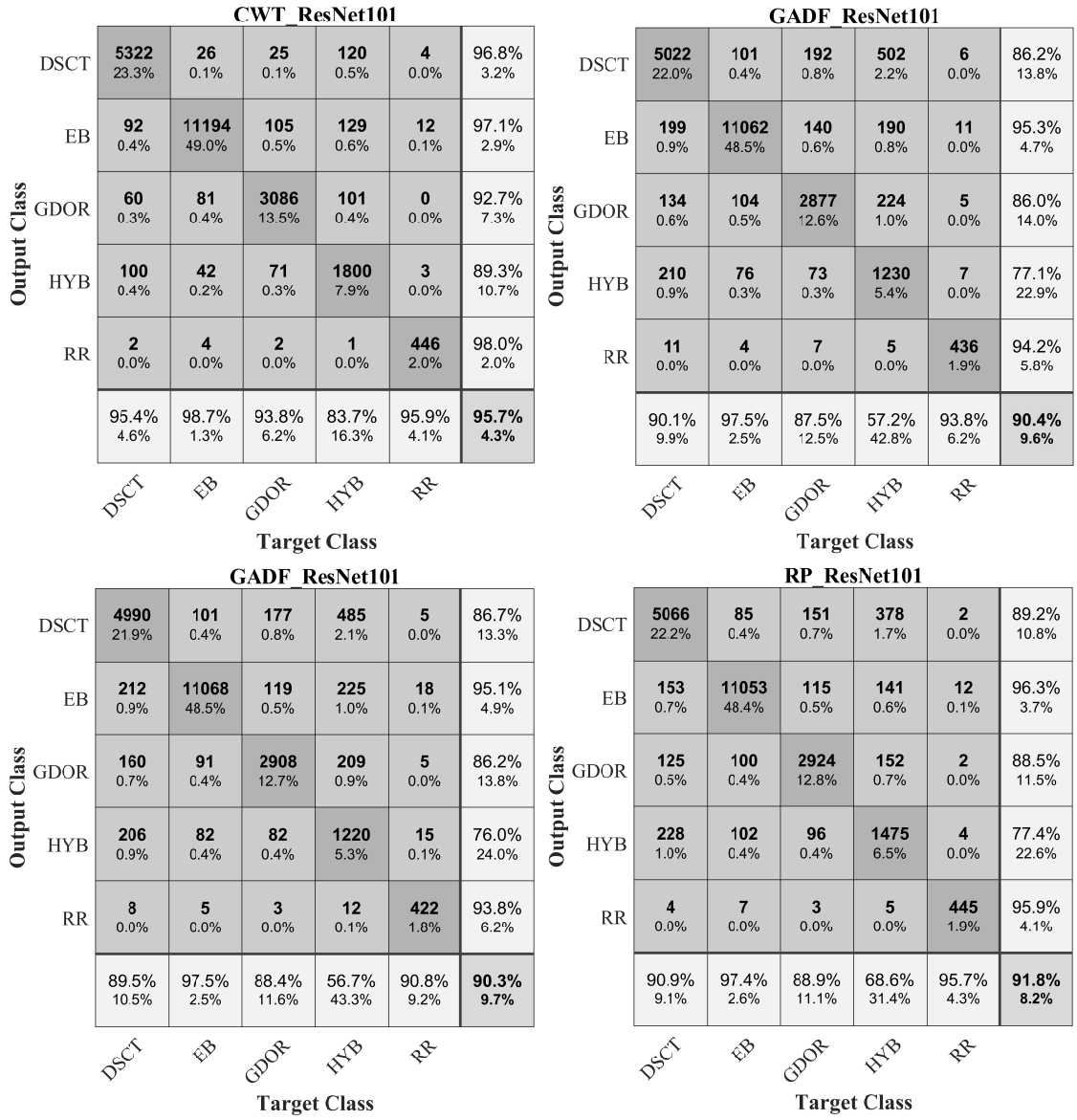


Fig. B.4. The confusion matrixes for ResNet101 architecture.

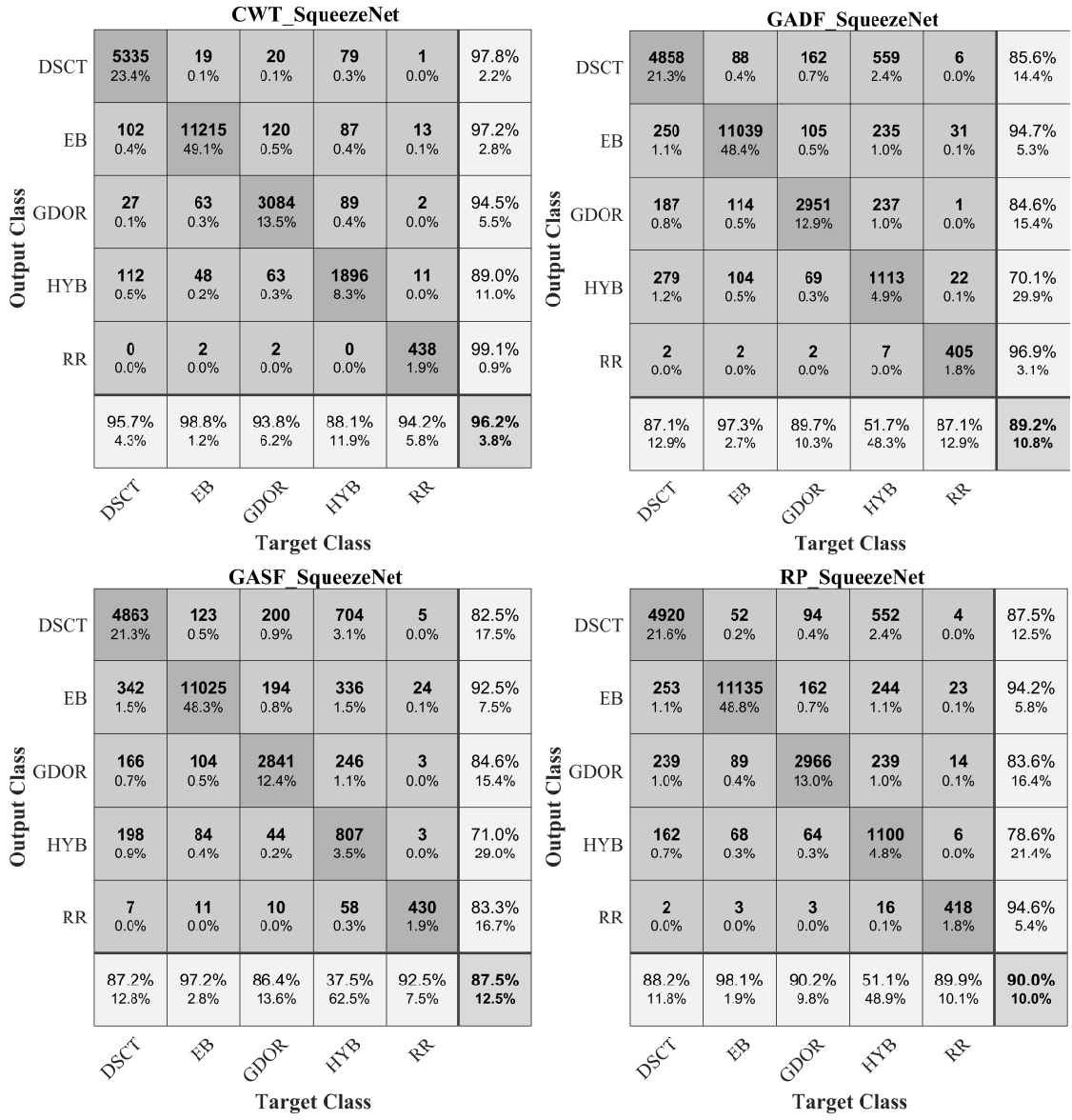


Fig. B.5. The confusion matrixes for SqueezeNet architecture.

		CWT_Xception					
Output Class	DSCT	5223 22.9%	25 0.1%	45 0.2%	149 0.7%	3 0.0%	95.9% 4.1%
	EB	133 0.6%	11165 48.9%	118 0.5%	134 0.6%	10 0.0%	96.6% 3.4%
	GDOR	81 0.4%	105 0.5%	3072 13.5%	195 0.9%	4 0.0%	88.9% 11.1%
	HYB	133 0.6%	46 0.2%	48 0.2%	1671 7.3%	4 0.0%	87.9% 12.1%
	RR	6 0.0%	6 0.0%	6 0.0%	2 0.0%	444 1.9%	95.7% 4.3%
		93.7% 6.3%	98.4% 1.6%	93.4% 6.6%	77.7% 22.3%	95.5% 4.5%	94.5% 5.5%
		Target Class					
		DSCT	EB	GDOR	HYB	RR	
		GADF_Xception					
Output Class	DSCT	4942 21.6%	90 0.4%	159 0.7%	588 2.6%	2 0.0%	85.5% 14.5%
	EB	193 0.8%	11058 48.4%	106 0.5%	181 0.8%	10 0.0%	95.8% 4.2%
	GDOR	206 0.9%	120 0.5%	2949 12.9%	229 1.0%	1 0.0%	84.1% 15.9%
	HYB	227 1.0%	75 0.3%	74 0.3%	1147 5.0%	15 0.1%	74.6% 25.4%
	RR	8 0.0%	4 0.0%	1 0.0%	6 0.0%	437 1.9%	95.8% 4.2%
		88.6% 11.4%	97.5% 2.5%	89.7% 10.3%	53.3% 46.7%	94.0% 6.0%	89.9% 10.1%
		Target Class					
		DSCT	EB	GDOR	HYB	RR	
		GASF_Xception					
Output Class	DSCT	4893 21.4%	101 0.4%	146 0.6%	631 2.8%	3 0.0%	84.7% 15.3%
	EB	264 1.2%	11054 48.4%	130 0.6%	261 1.1%	20 0.1%	94.2% 5.8%
	GDOR	221 1.0%	112 0.5%	2954 12.9%	251 1.1%	3 0.0%	83.4% 16.6%
	HYB	193 0.8%	77 0.3%	54 0.2%	992 4.3%	22 0.1%	74.1% 25.9%
	RR	5 0.0%	3 0.0%	5 0.0%	16 0.1%	417 1.8%	93.5% 6.5%
		87.8% 12.2%	97.4% 2.6%	89.8% 10.2%	46.1% 53.9%	89.7% 10.3%	89.0% 11.0%
		Target Class					
		DSCT	EB	GDOR	HYB	RR	
		RP_Xception					
Output Class	DSCT	4944 21.7%	112 0.5%	111 0.5%	509 2.2%	1 0.0%	87.1% 12.9%
	EB	200 0.9%	10995 48.2%	100 0.4%	164 0.7%	12 0.1%	95.9% 4.1%
	GDOR	184 0.8%	126 0.6%	2979 13.0%	222 1.0%	7 0.0%	84.7% 15.3%
	HYB	243 1.1%	111 0.5%	95 0.4%	1252 5.5%	9 0.0%	73.2% 26.8%
	RR	5 0.0%	3 0.0%	4 0.0%	4 0.0%	436 1.9%	96.5% 3.5%
		88.7% 11.3%	96.9% 3.1%	90.6% 9.4%	58.2% 41.8%	93.8% 6.2%	90.3% 9.7%
		Target Class					
		DSCT	EB	GDOR	HYB	RR	

Fig. B.6. The confusion matrixes for Xception architecture.

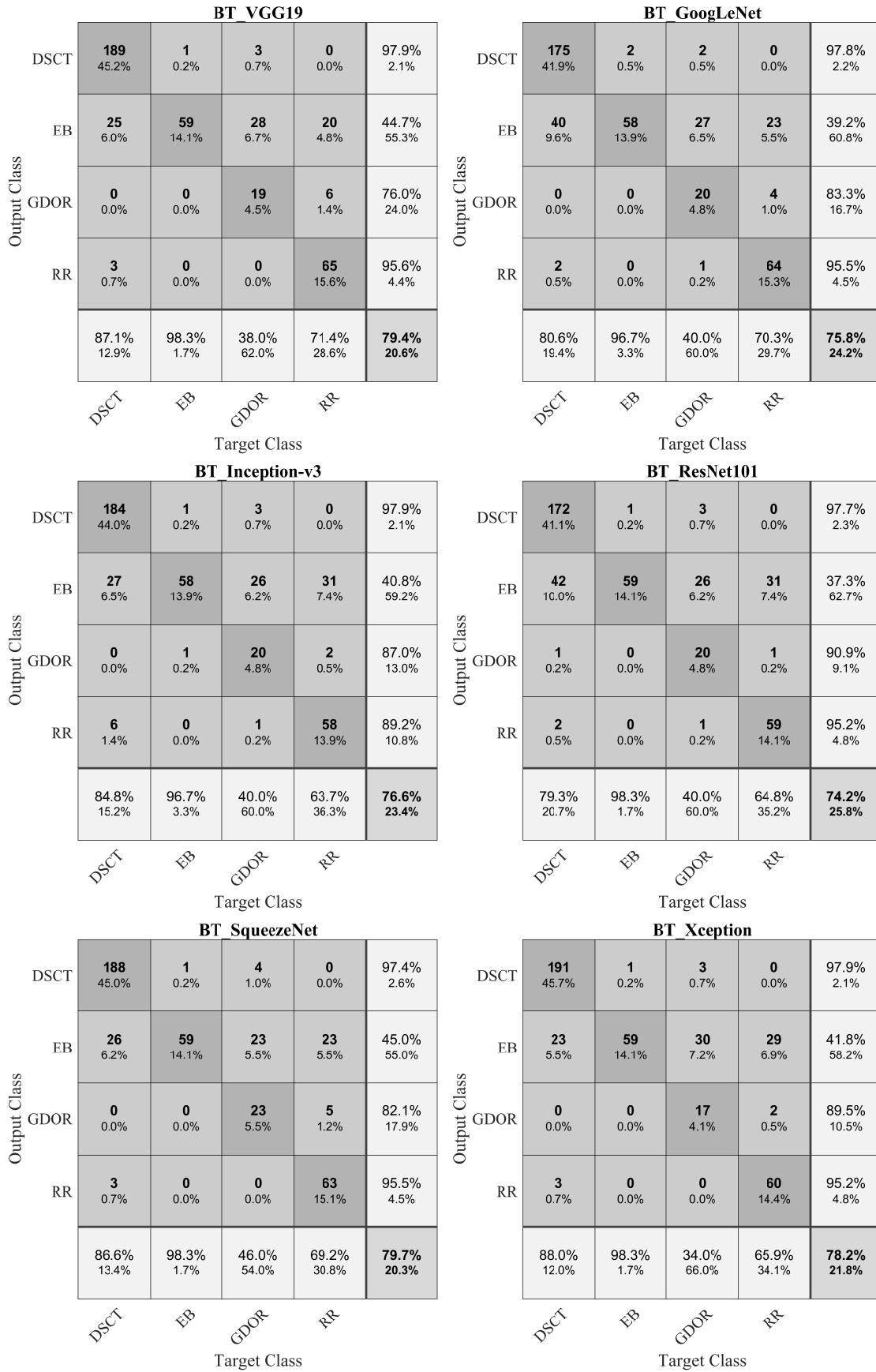


Fig. C.1. The confusion matrixes for blind tests.